Utrecht University

Debye Institute for Nanomaterials Science

Quantum Nanophotonics Group

Femtosecond laser nano-ablation of glass surfaces and their self-scattering effects

Author:

Jasper Clarijs B.Sc.

Supervisors:

Dr. F.J. Hernández-Rueda
Prof. dr. D.M. Krol
Dr. D. van Oosten

March 9, 2016

Abstract

In this thesis, the interaction between a femtosecond laser and glasses in the ablation regime is studied. A pulsed femtosecond laser setup allows for surface ablation of glasses under strong focussing conditions. This setup is used to measure the reflectivity of four different glasses as a function of the laser fluence, in order to study the self action of the laser pulse. The craters produced by the laser pulse are examined using atomic force microscopy. These two measurements together are able to provide insights in the energy coupling of the laser pulse into the material. It is found that for increasing fluences, the self-reflectivity and crater depth both rise with increasing slopes. With a similar experimental setup, which uses a pump and probe technique, the dynamics of femtosecond laser matter interaction in fused silica are studied under weak focussing conditions. By illuminating the plasma generated by the pump beam at different times using a delayed probe beam, its evolution can be observed by its reflectivity. It is seen that in $\sim 1\,\mathrm{ps}$, the plasma reaches its maximum reflectivity. The plasma's reflectivity remains constant for several picoseconds, before recombining with the glass. Well after the laser has interacted with the glass, signs of material ablation can be observed. A one-dimensional finite-difference time-domain simulation is performed to replicate the experiment's results. The simulation applies the Drude model and the often used single rate equation developed by Stuart *et al.* to model ionization. The simulated results do not agree with the experimental results, due to an overestimation of the ionization rate by the single rate equation. Instead, implementation of a multiple rate equation is suggested to model ionization.

Contents

1 Introduction

Ever since its invention by Theodore Maiman of Hughes Laboratories in May 1960[1], lasers have found wide-spread applications in academia, healthcare, industry, household appliances and even art. In laboratories all over the world lasers are used in imaging techniques, laser cooling[2], and waveguide writing[3,4], just to name a few. A world without lasers is unimaginable these days, and the laser has come a long way since the first pulsed laser from the sixties. Nowadays, many laser characteristics, such as wavelength, power, pulse duration, pulse shape and more can be chosen with only few constraints. This has lead to multiple distinct subfields of research.

One of these fields considers laser pulses of extremely short durations and thus extremely high peak intensities. Pulse durations of the order of 10^{-15} s and intensities of the order of 10^{14} $\mathrm{W/cm^2}$ are not uncommon. This type of pulse is interesting because they consist of electric fields of the same order of magnitude as the fields that electrons in an atom experience due to the Coulomb field of an atom's nucleus. Hence they are capable of changing the morphology of even high-band gap materials in a well-confined region.

One generic application of ultrashort laser pulses is ablation, where material is removed by the pulse. Because of the low pulse duration, the electromagnetic interaction is well separated from any thermal interaction in the material, and ablation happens deterministically. This can be used to remove tumor material[5], write waveguides, and for surface modification.

For this thesis the interaction of single femtosecond laser pulses incident on glass surfaces under ablating conditions is studied. The project is a collaboration between Utrecht University and University of California, Davis, enabled by professor Denise Krol. The motivation for this study is to understand the energy coupling of a laser pulse into insulator material, and how this affects the surface nanostructuring due to the laser action. Specifically three zinc-phosphate glasses doped with different aluminiumoxide concentrations and fused silica are studied. Earlier works in the group of Dr. van Oosten done by dr. Hao Zhang and Stephan Wolbers, MSc have studied the interactions of a femtosecond laser pulse with a semiconductor[6] and a metal[7], respectively. This work on insulators will contribute in understanding femtosecond laser-matter interaction more completely. The laser-matter interaction is studied by looking at the changes in reflectivity of the glasses due to the pulse, both temporally resolved and temporally integrated. Also the craters produced by the laser pulse are observed and their morphology is measured.

In the second section of this thesis, the general theory of a femtosecond laser pulse interacting with an insulator is discussed. This will introduce relevant aspects of laser pulse propagation, laser-matter interaction through the dielectric constant, and plasma formation through different ionization mechanisms. In the third section,

the experiment ablating nano-craters on the glass surfaces is explained and its results are presented. The fourth section considers the transient reflectivity measurements obtained via the pump-probe experiment performed in Davis. Next, in the fifth section, a simulation of the pump-probe experiment is explained. Lastly, in the final section the most important conclusions are summarized and an outlook of possible follow-up research is discussed.

2 Theory of femtosecond laser-matter interaction

In this section, the theory that describes the interaction of an intense laser pulse with a glass material is introduced. In order to understand the energy coupling of an intense laser into glass, first electromagnetic wave propagation will be considered. Inside the glass, there will be nonlinear laser-matter interaction. Because the photon energy of the 800 nm laser that is used is 1.55 eV, but the bandgap of e.g. fused silica can be up to 9 eV, only very intense fields interact significantly. This results in a hot electron plasma through several ionization mechanisms, which will be discussed. The plasma affects how the laser pulse propagates through the glass and how it is partially reflected back. The theory about electromagnetic fields, ionization and pulse propagation in the plasma will be used mostly in the simulation described in Section 5. As a result of the plasma, the surface material is ablated. This surface ablation is thought to happen well after the pulse is over, so it does not have to be considered during the simulated laser-matter interaction.

2.1 Electromagnetic wave propagation

Consider the propagation of the electromagnetic wave. In both vacuum and glass, the behaviour of the electromagnetic fields is described by Maxwell's equations[8]

$$\nabla \cdot \mathbf{D} = \rho_{\mathrm{f}}, \tag{2.1}$$

$$\nabla \cdot \mathbf{B} = 0, \tag{2.2}$$

$$\nabla \times \mathbf{E} = -\frac{\partial \mathbf{B}}{\partial t}, \tag{2.3}$$

and

$$\nabla \times \mathbf{H} = \mathbf{J_f} + \frac{\partial \mathbf{D}}{\partial t}, \tag{2.4}$$

where $\mathbf{E}$, $\mathbf{B}$, $\mathbf{D}$ and $\mathbf{H}$ stand for the electric field, magnetic field, displacement field and magnetizing field respectively. $\mathbf{J_f}$ denotes the current of free charges and ρ_{f} denotes the free charge density. The constitutive relations for isotropic and homogeneous media are expressed using the relative dielectric function ϵ and relative permeability μ as

$$\mathbf{D} = \epsilon\epsilon_0\mathbf{E} \tag{2.5}$$

and

$$\mathbf{H} = \frac{1}{\mu\mu_0}\mathbf{B}. \tag{2.6}$$

Here ϵ_0 and μ_0 denote the permittivity and permeability of the vacuum respectively. Eqs. 2.1-2.6 govern all behaviour of the electromagnetic field in- and outside the

glass material, and therefore also the laser pulse propagation. Since for any optical material $\mu = 1$, only ϵ need be considered. In this model, the complex quantity ϵ incorporates all effects that the laser pulse has on the material, and how the material in turn influences the propagation of the pulse. For a plasma inside a glass, a Drude-like model is used to parameterize the relative dielectric function

$$\epsilon = \bar{n}^2 - \frac{e^2\tau}{m_{\text{eff}}\omega\epsilon_0\,(i+\omega\tau)}\rho. \tag{2.7}$$

Here $\bar{n}$ stands for the glass' index of refraction, e the elementary electron charge, τ the electron collision time, m_{eff} the effective mass of a free electron, ω the laser frequency and ρ the free electron number density. The glass' index of refraction is calculated using the ordinary refractive index n_0 and a contribution due to the Kerr effect, namely

$$\bar{n} = n_0 + n_2 I. \tag{2.8}$$

Here n_2 is the Kerr-effect coefficient and I the laser intensity. Eq. 2.8 is valid for centrosymmetric materials as long as the nonlinear contribution remains small compared to the ordinary contribution. From Eqs. 2.7 and 2.8 it can be seen that in the absence of a pulse and a plasma ($I = 0$,$\rho = 0$), the dielectric function reduces to the well-known relation $\epsilon = n_0^2$. Since in the experiments the prefactor $\frac{e^2\tau}{m_{\text{eff}}\omega\epsilon_0} = 1.35 \times 10^{-27}\,\text{m}^3$, very large free electron densities are required to affect the propagation of light (estimating $\tau = 1\,\text{fs}$, $m_{\text{eff}} = 1\,\text{m}_\text{e}$).

2.2 Ionization mechanisms

There are three relevant ionization mechanisms that create a plasma during the experiments. They are multi-photon ionization (MPI), tunneling ionization (TI) and avalanche ionization (AI), illustrated in Fig. 2.1. MPI loosely speaking corresponds to when an electron in the valence band absorbs enough photons simultaneously to bridge the band gap of the material. TI is possible when the applied electric field lowers the molecules' Coulomb potential enough for an electron to tunnel through the remaining potential. For over-the-barrier ionization the Coulomb potential is lowered enough that the electron has a significant probability of crossing over to the conduction band freely. For the intensities applied in our experiments, over-the-barrier ionization need not be considered. Avalanche ionization happens in two steps: first, an electron in the conduction band absorbs incoming radiation through inverse Bremsstrahlung. Then when this electron has gained enough energy, it can collide with an electron in the valence band to excite it to the conduction band.

2.2.1 Keldysh' theory of strong field ionization

Both MPI and TI are two examples of a more general strong field ionization (SFI) process. The rates at which SFI occurs was first theoretically described by Keldysh[11],

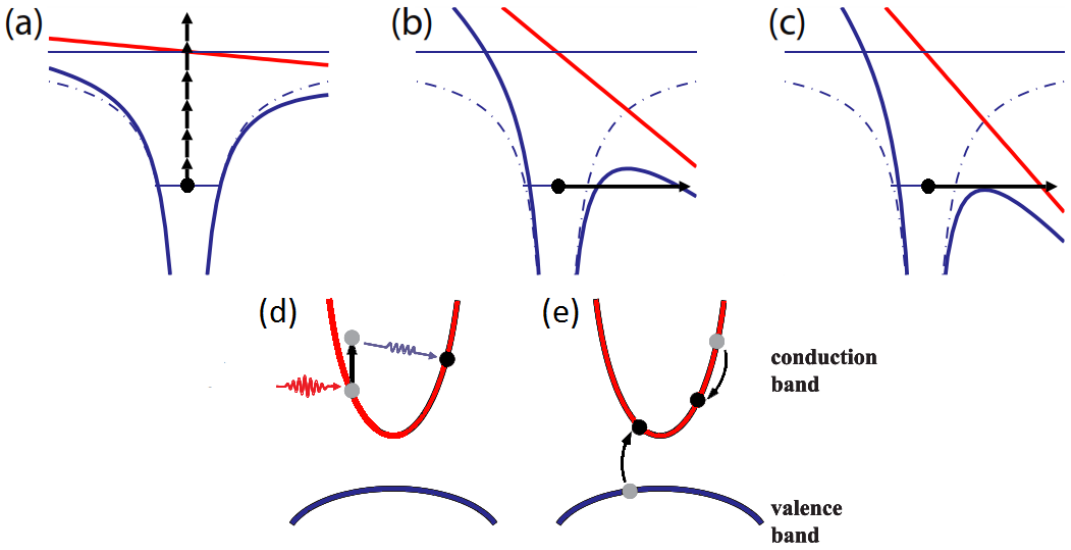

Figure 2.1: Different possible ionization mechanisms for insulators. Solid red lines indicate the conduction band, solid blue lines indicate the valence band. (a) Multi-photon ionization. (b) Tunneling ionization. (c) over-the-barrier ionization, which does not occur significantly for our intensities. (d) Intraband absorption through inverse Bremsstrahlung. (e) Impact ionization. Images adapted from Balling[9] and Mao[10].

and later corrected by Gruzdev[12]. Keldysh' theory assumes the dispersion relation

$$E(p) = \Delta \left(1 + \frac{p^2}{m_{\mathrm{red}}\Delta}\right)^{1/2}, \tag{2.9}$$

where $E(p)$ denotes the energy of an electron as a function of its momentum p, reduced effective mass m_{red} and band gap Δ. Whether MPI or TI is the dominant process depends on the so-called Keldysh parameter $\gamma = \frac{\omega\sqrt{m_{\mathrm{red}}\Delta}}{eE}$ (E-electric field strength), which is roughly the ratio between the tunneling time and one optical period. When the tunneling time is bigger than the optical period, the electron will simply not have enough time to cross the lowered barrier before the field stops lowering the barrier sufficiently. Thus when $\gamma \ll 1$ TI dominates and when $\gamma \gg 1$ MPI dominates. The expression for the resulting ionization rate, as corrected by Gruzdev[12], is

$$W_{SFI} = \frac{4\omega}{9\pi}\left(\frac{m_{\mathrm{red}}\omega}{\hbar\sqrt{\gamma_1}}\right)^{3/2} Q(\gamma, x) \times \exp\left(-\pi\lfloor x+1\rfloor \frac{\mathcal{K}(\gamma_1) - \mathcal{E}(\gamma_1)}{\mathcal{E}(\gamma_2)}\right), \tag{2.10}$$

with

$$Q(\gamma, x) = \sqrt{\frac{\pi}{2\mathcal{K}(\gamma_2)}} \times \sum_{n=0}^{\infty} \exp\left(-n\pi \frac{\mathcal{K}(\gamma_1) - \mathcal{E}(\gamma_1)}{\mathcal{E}(\gamma_2)}\right) \times \Phi\left(\pi\sqrt{\frac{\lfloor x+1\rfloor - x + n}{2\mathcal{K}(\gamma_2)\mathcal{E}(\gamma_2)}}\right). \tag{2.11}$$

Here $\gamma_1 = \frac{\gamma^2}{1+\gamma^2}$, $\gamma_2 = \frac{1}{1+\gamma^2}$ and $x = \frac{2}{\pi}\frac{\Delta}{\hbar\omega}\frac{\mathcal{E}(\gamma_2)}{\sqrt{\gamma_1}}$ (the effective band gap in units of photon energy). $\mathcal{K}$ and $\mathcal{E}$ denote the complete elliptic integrals of the first and second kind, Φ is the Dawson integral, and $\lfloor x \rfloor$ stands for the floor function of x. For an 800 nm laser hitting a material with a band gap of 9 eV, the strong field ionization rate is plotted against electric field strength in fig. 2.2.

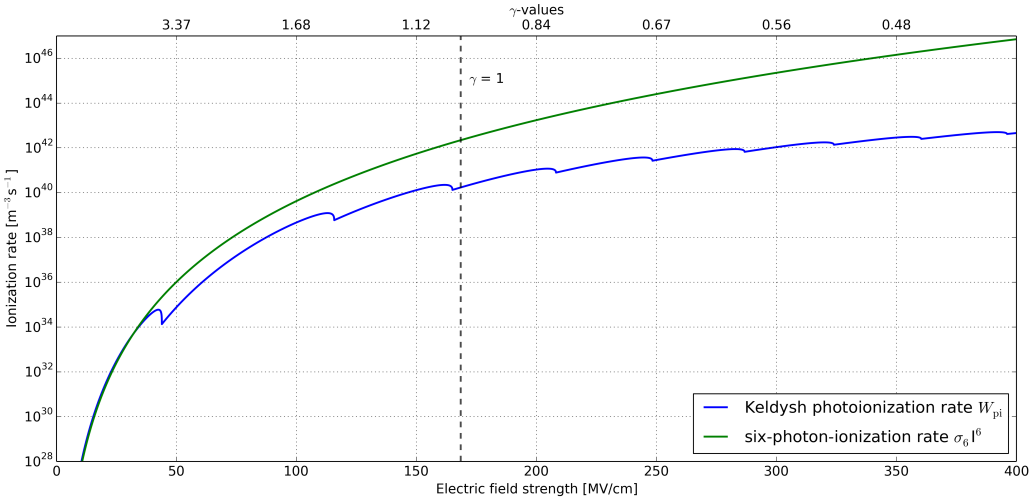

Figure 2.2: Keldysh ionization rates as a function of electric field strength. A fit to $W_{\mathrm{MPI}} = \sigma_6 I^6$ is also shown, and $\sigma_6 = 8.188 \times 10^{-65}\,(\mathrm{W/m^2})^{-6}\,\mathrm{m^{-3}s^{-1}}$ is found.

Note the bumps in the Keldysh ionization rates, which are caused by the floor function in Eq. 2.11. They correspond to the increase of the effective band gap $U'_{\mathrm{eff}} = x\hbar\omega$ as a result of the ponderomotive energy U_{p}. Since[13]

$$U'_{\mathrm{eff}} = \frac{2\Delta}{\pi}\frac{\mathcal{E}(\gamma_2)}{\sqrt{\gamma_1}} \simeq \Delta + U_{\mathrm{p}} = \Delta + \frac{e^2E^2}{4m_{\mathrm{red}}\omega^2}, \tag{2.12}$$

the higher the field, the larger the effective band gap.

It can be shown[9] that in the low field limit, the Keldysh ionization rates will scale with I^6. In Fig. 2.2 a fit is also plotted, and it can be seen that this fit is no longer valid for field strengths higher than $50\,\mathrm{MV/cm}$. The highest electric field of the laser pulse reached during our experiments is near $200\,\mathrm{MV/cm}$, which corresponds to $\gamma = 0.84$, meaning we are in the cross-over regime between MPI and TI. Only the full expression 2.10 is thus applicable.

It should be noted that several authors have found and applied different values for the ionization rates in experiments in the MPI limit. Lenzner *et al.* have found that $\sigma_6 = 6.0 \times 10^{-70}\,(\mathrm{m^2/W})^6\,\mathrm{m^{-3}s^{-1}}$, while Li *et al.* found $\sigma_6 = 3.0 \times 10^{-74}\,(\mathrm{m^2/W})^6\,\mathrm{m^{-3}s^{-1}}$, in contrast to the fitted value of $\sigma_6 = 8.2{\times}10^{-65}\,(\mathrm{m^2/W})^6\,\mathrm{m^{-3}s^{-1}}$. The values for the MPI coefficient differ several orders of magnitude from each other

and from the one derived form Keldysh' theory. Nonetheless, Keldysh' theory has been used in several works considering ionization of dielectrics by intense lasers[13–19].

2.2.2 Avalanche ionization

The other relevant ionization mechanism is AI. An often used expression for the AI rate was derived by Stuart et al. based on the solution of the Fokker-Planck equation for the electron distribution function[18]. A rate linearly proportional to the intensity and free electron density was found:

$$W_{\mathrm{AI}} = \beta I \rho, \tag{2.13}$$

where the prefactor β is a constant calculated by solving their kinetic equations numerically. Stuart *et al.* found a value of $11\,\mathrm{cm^2/J}$ for fused silica with a band gap of 9 eV. Other authors have applied Joule heating to an electron gas to come to the same conclusion, namely an AI rate linearly proportional to the laser intensity and free electron density. For this derivation, see appendix A. The resulting formula for β is

$$\beta = \frac{\Omega}{U_{\mathrm{eff}}}. \tag{2.14}$$

Here

$$\Omega = \frac{1}{n_0 c \epsilon_0} \frac{e^2 \tau}{m_{\mathrm{red}}(\omega^2\tau^2 + 1)} \tag{2.15}$$

(with c the speed of light) is the single electron inverse Bremsstrahlung cross section, and

$$U_{\mathrm{eff}} = \left(2 - \frac{m_{\mathrm{red}}}{m_{\mathrm{e}}}\right)\left(\Delta + \frac{e^2E^2}{4m_{\mathrm{red}}\omega^2}\right) \tag{2.16}$$

is the critical energy necessary to collisionally excite a conduction band electron across the band gap Δwhile fulfilling energy *and* momentum conservation[13] . Intuitively it makes sense that the AI rate depends on the free electron density (more electrons to absorb radiation means more electrons to collisionally excite valence band electrons) and the laser intensity (more radiation to be absorbed).

For our experiment, the scattering time and effective mass are estimated to be $\tau = 1\,\mathrm{fs}$ and $m_{\mathrm{eff}} = 1\,\mathrm{m_e}$. The theoretical value of the avalanche ionization coefficient is then $\beta = 7.7\,\mathrm{cm^2/J}$, which is in reasonable agreement with Stuart's value. However, more discrepancies between these avalanche ionization coefficients can be found, as is displayed in Table 2.1. The differences among the three coefficients calculated with Eq. 2.14 lie in the choices of τ and m_{eff}. Even though the scattering time τ is temperature-dependent, a pulse-averaged value is often assumed. Similarly, the effective electron mass m_{eff} depends on the potential landscape in the neighbourhood of the conduction electrons, but is often assumed to be $m_{\mathrm{eff}} = 1\,\mathrm{m_e}$.

Author	β [cm^2/J]	Method of calculation
Stuart *et al.*	11	Numerical calculation of Fokker-Planck equation
Lenzner *et al.*	4.0	Experimentally found
Sudrie *et al.*	9.0	Joule heating calculation (Eq. 2.14)
Wu *et al.*	7.9	Joule heating calculation (Eq. 2.14)
This work	5.2	Joule heating calculation (Eq. 2.14)

Table 2.1: Values for the avalanche ionization coefficient β as found by different authors. Note that when the Joule heating calculation is applied, that $U_{\text{eff}} = U_{\text{g}} = 9\,\text{eV}$.

2.2.3 The rate equation

Including both the SFI and AI rates, the evolution of the electron density is described with the rate equation

$$\frac{d\rho}{dt} = (W_{\text{SFI}} + \beta I \rho)\left(1 - \frac{\rho}{\rho_{\text{max}}}\right) - \frac{\rho}{\tau_{\text{s}}}. \tag{2.17}$$

Here saturation of the plasma is accounted for by only allowing a maximum electron density of ρ_{max}. This term could be chosen to correspond to the glass molecule density[16], the glass' atom density[20], or other specific criteria[21]. Recombination and self-trapping[22] may also be considered by including exponential decay with the last term $-\frac{\rho}{\tau_{\text{s}}}$. Here τ_{s} denotes the $1/e$ decay time of electrons decaying back into the valence band and/or self-trapping states. Whether these effects are actually taken into account in the performed simulations is discussed later in Section 5.

2.3 Experiments: reflectivity and ablation

In the experiments, the glasses' reflectivity is measured, both time-integrated and time resolved. Theoretically, the reflectivity R of the glass-air interface under normal incidence can be calculated using the Fresnel equation[23]

$$R = \left(\frac{|\widetilde{k_1} - \widetilde{k_2}|}{|\widetilde{k_1} + \widetilde{k_2}|}\right)^2. \tag{2.18}$$

Here $\widetilde{k_1}$ and $\widetilde{k_2}$ denote the complex wavenumbers of the wave in air and in excited glass respectively. Hence the reflectivity depends on the dielectric function and therefore the free electron density of the material. The higher the electron density, the higher the reflectivity. However in both the time-integrated case and the time-resolved case, the reflectivity cannot be calculated as straightforwardly as Eq. 2.18 suggests. The

reason for this is that both the pulse intensity and thus also the dielectric function are a function of time. Since the lifetime of the plasma is longer than the pulse duration and the reflectivity is not constant during the pulse, the actual amount of reflected light has to be calculated with a more complicated integral of the form

$$F_{\mathrm{rfl}} = \int_0^T I(t)R(t)dt. \tag{2.19}$$

Here the time-dependent intensity $I(t)$ and reflectivity $R(t)$ would have to be multiplied and integrated over a suitable time interval T to find the reflected fluence F_{rfl}. To complicate things even further, the depth dependent electron density causes a depth dependence in reflectivity as well. In order to fully take into account the effects of space- and time-dependent reflection off of the plasma, the entire plasma generation and pulse-plasma interaction are modelled in a Finite-Difference Time-Domain (FDTD) simulation. This will be discussed in greater detail in Section 5.

After the laser pulse has interacted with the glass, thermal effects will come into play. The plasma is in a non-equilibrium state of high pressure and high temperature, leading to an unstable lattice. Separation of charges due to ionization causes high Coulomb repulsion. These effects result in a Coulomb explosion, ejecting matter from the surface and leaving behind a crater. Because the electromagnetic interaction is thought to happen much sooner than any thermal process, craters are created deterministically instead of statistically. This is summarized in Fig. 2.3, which also shows the timescales and intensity-dependency leading up to ablation for semiconductors and metals.

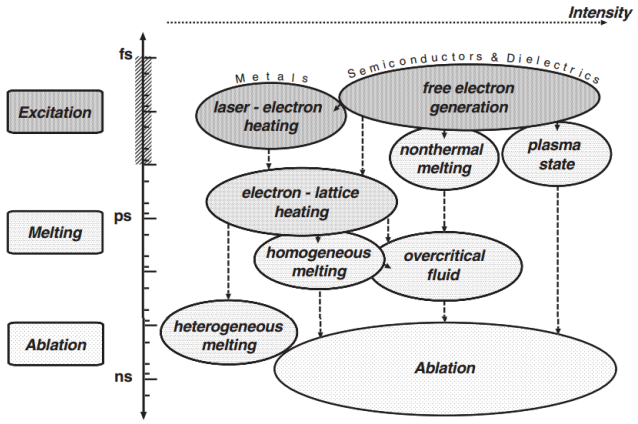

Figure 2.3: Processes and their timescales leading to ablation for different material types. Image taken from Rethfeld[24].

In the following two sections, the experimental results on ablation and reflectivity will be presented.

3 Ablation and selfreflectivity under strong focussing conditions

For this study the interaction of an intense laser with glasses is studied via two ways. One way is by looking at the reflectivity of the glass, which changes as a result of plasma formation in the glass. This provides us with fundamental insight into plasma formation and thus information on how energy couples into the glass. The other way to study the interaction is by considering the ablated craters resulting from the laser pulse. Studying these craters is important for application in nanofabrication. Additionally, it provides lots of insight into the underlying physics that lead to crater formation and thus again energy coupling. In this experiment the laser is tightly focussed onto the material. This has the advantage that less power is needed to obtain high peak intensity. It also allows for sub-diffraction-limited features, since the laser only creates a plasma where the local fluence crosses a certain ablation threshold. Only past this threshold will the plasma be dense and hot enough for ablation to occur. In this section, first the experimental setup allowing us to study these glasses and their ablated surface nanostructures is described. Next the experiments' results and conclusions are presented, and finally suggestions for improvements to the setup are discussed.

3.1 Experimental setup and parameters

The experimental setup used is shown in Fig. 3.1. A Titanium Sapphire regenerative amplifier system (Hurricane, Spectra-Physics) fires single 800 nm, 450 fs linearly polarized laserpulses with a maximum energy of 1 mJ and maximum repitition rate of 1 kHz. One such pulse passes a half-wave plate ($\lambda/2$) and consequently a polarizing beamsplitter cube (PBS), which allows us to control the energy that passes through. One part of the pulse is then split off and blocked by a beam block (BB). The other part, after passing a mechanical shutter (Uniblitz Electronic VS14S2T1), is then aimed through a telescope. Here it is collimated in such a way that the laser pulse' focus coincides with the camera's focus. After the telescope the pulse is split up again into a reference beam (ref. beam, dotted red line) and a pump beam. The reference beam does not hit the sample, but instead is aimed at a 12 bit CCD camera (Qimaging RETIGA 1300) directly after passing a neutral density (ND, OD = 0.62) filter and a tube lens (TL, 300 mm). The pump beam passes another beam splitter, a pellicle mirror (PM) through its non-reflective side, and then finally a microscope objective (MO, Nikon CFI60, NA = 0.8, 100x, working distance 3.5 mm) which focusses the pulse on the sample surface. The MO has a numerical apperture of 0.8, resulting in a very tight focus (focal diameter ~1 μm). The MO can be moved with a translation stage (Zaber Tech T-LSM025A) in the vertical (Z) direction, the sample can be positioned in the horizontal plane (XY) with another stage (PIline

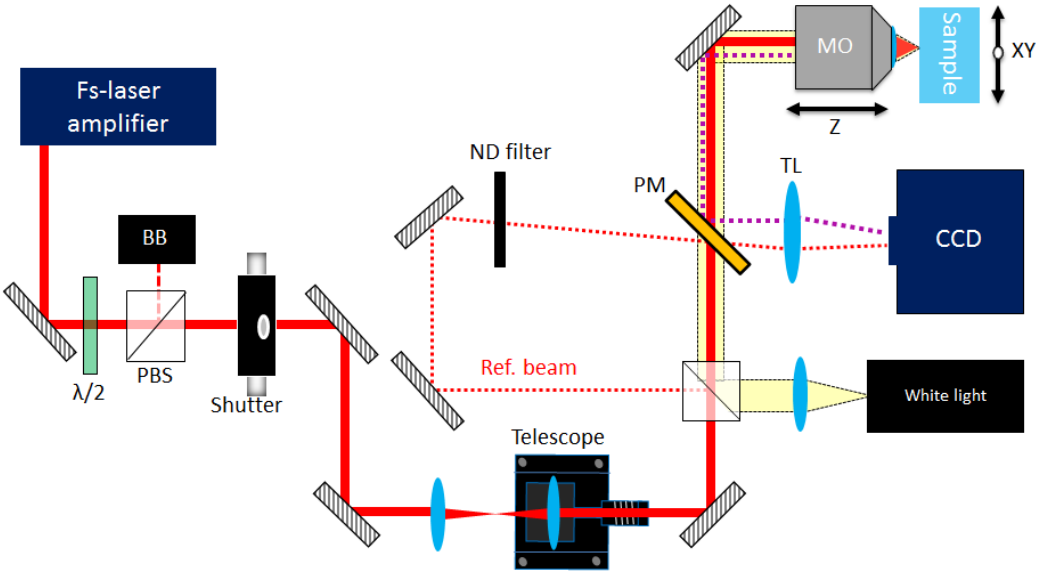

Figure 3.1: Experimental setup allowing for controlled fabrication of surface nano-craters and observation of reflected beamprofiles of glass. Dashed rectangles represent mirrors, blue ovals represent lenses.

M-686.D64). The laser pulse is reflected off the glass sample surface (dotted purple line), reflected by the reflective side of the pellicle mirror, and finally focussed onto the CCD camera by the tube lens. Additionally, a white light source illuminates the sample surface to aid with targetting and focussing.

The experimental parameter that is being varied for this study is the pulse energy, and therefore the fluence. The fluence F is defined as the time-integrated intensity. Peak fluence for Gaussian pulses can be calculated using $F = \frac{E}{A_{\text{eff}}}$, where E is the pulse energy and A_{eff} is the effective spotsize of the laser. This effective spotsize is determined by the radius where the $1/e$ intensity value of the spot is attained. It is found to be of the order of $0.5\,\mu$m during our experiments. Fluence is the quantity of interest, since ablation is a result of a high electron density. This density is caused by a transient intensity (Eq. 2.17) over the course of a pulse. Hence just the pulse energy does not provide enough information about the type of pulse used. Instead, the peak fluence and pulse duration are specified. Both the pulse energy and effective spotsize can be determined with the CCD camera, which captures both the reflected beamprofile and the reference beamprofile. These results will be discussed in more detail in Section 4. By moving the MO in the Z direction, the sample surface is brought into focus. By moving the sample with the XY translation stage a fresh spot without visible surface defects is picked. For several different pulse energies, twenty irradiations are performed in a row. If the fluence is above the so-called ablation threshold, craters are produced, resulting in an array of craters with increasing energies along one of its sides. After each irradiation the sample is moved

Sample reference	Composition	Refractive index
ZAP1	60% ZnO 40% P_2O_5	1.458
ZAP2	51% ZnO 44% P_2O_5 5% Al_2O_5	1.458
ZAP3	42% ZnO 48% P_2O_5 10% Al_2O_5	1.458
FS	SiO_2 (Fused silica, Corning 7980)	1.4533[25]

Table 3.1: Glass sample properties.

by 2 μm to ensure the pulse hits a fresh spot. The frequency of irradiations is 2 Hz, so that the translation stages are no longer vibrating from moving at the time the sample is irradiated[6]. The samples chosen for this study are three zinc-phosphate glasses doped with aluminium (ZAP glasses) and fused silica. The ZAP glasses are chosen because they may be suitable for waveguide writing, and fused silica is chosen because it is a good model dielectric that has been studied much before. The band gap for fused silica is 9 eV, and for the ZAP glasses it is < 5 eV. The samples' other properties are listed in Table 3.1.

3.2 Powercalibration

Using the reference beam, it can be determined how much energy arrives at the sample. For this, the pixel values of the reference beam are summed up and related to a pulse energy (for an example of a reference beam as captured by the CCD camera, see Fig. 3.3). This relation is determined by putting a power meter (Newport 818-SL) in place of the sample. By setting the repetition rate of the laser to 1 kHz, the average power of 1000 pulses is measured. For different measured powers, twenty reference beam profiles are captured by the CCD camera. These twenty profiles are averaged and a pixel sum is taken. The value of this pixelsum is then paired with the power measured by the power meter. This power can be converted into a pulse energy by dividing by the repetition rate. This calibration is performed twice, where the second time an extra ND filter (OD = 0.3) is put in the reference beam path in order to prevent saturation of the camera at high intensities. The resulting (summed pixel intensity, pulse energy)-plot is shown in Fig. 3.2. Theoretically, a linear relation between pixelsum (which is supposedly a time- and space-integrated intensity) and pulse energy is expected. Obviously this is not the case, and we attribute this error to the use of a faulty power meter. Nonetheless, an approximate relation between the quantities can still be established. The summed pixel intensity is fitted to the pulse energy using $f(x) = ax^2 + bx$, and the fits are shown the same figure as the data.

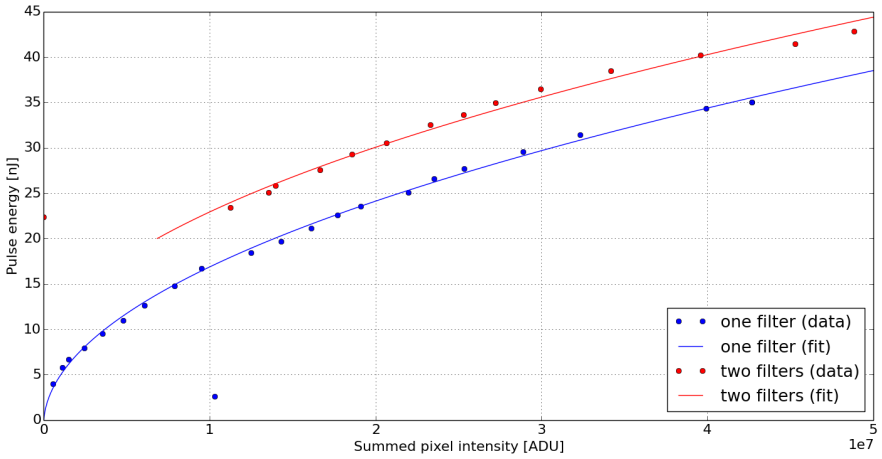

Figure 3.2: Calibration of the power meter against the reference beam's summed pixel intensity. The inverse relation is fit to $f(x) = ax^2 + bx$ and used to calibrate the pulse energy arriving at the sample during our experiment. The one filter fit parameters are $a = 3.3 \times 10^4 \pm 0.6 \times 10^4$ and $b = 4.3 \times 10^4 \pm 1.4 \times 10^4$. The two filters fit parameters are $a = 3.2 \times 10^4 \pm 0.2 \times 10^4$ and $b = -3.0 \times 10^5 \pm 5.6 \times 10^4$.

3.3 Results: selfreflectivity

The way electromagnetic energy from the laser couples into the glass is largely affected by how the laser's action on the material. One way of studying this energy coupling is by looking at the amount of light that is reflected off of the sample. This was done for different energies for the four samples described in Table 3.1. Fig. 3.3 shows an example of a captured reflected beam profile and its corresponding reference beam profile. Here a background subtraction was already applied. Using the reference beam and the power meter calibration, the pulse energy ariving at the sample is determined. For the fluence, the beam waist is also required. This is found by fitting the beam profile to a Gaussian profile

$$G(x, y) = A \exp\left[-\left(\frac{x - x_0}{w_\mathrm{x}}\right)^2 - \left(\frac{y - y_0}{w_\mathrm{y}}\right)^2\right] - B. \tag{3.1}$$

Here A corresponds to the peak value of the laser pulse, x_0 and y_0 are the spatial offsets of the laser, w_x and w_y are the beam waists, and B is the background value (which, after background subtraction, should be zero). On average, the beam waist of the focussed laser is $510 \pm 4\,\mathrm{nm}$. The effective area is then $A_\mathrm{eff} = \pi w_\mathrm{x} w_\mathrm{y}$. For every individual pulse, the fluence is calculated using the area from a Gaussian fit and the energy observed using the reference beam. For high energies, the reflected beam profiles have flattened tops as can be seen in Fig. 3.4. This could either be due to a distored reflection of the Gaussian profile, or due to camera saturation. During

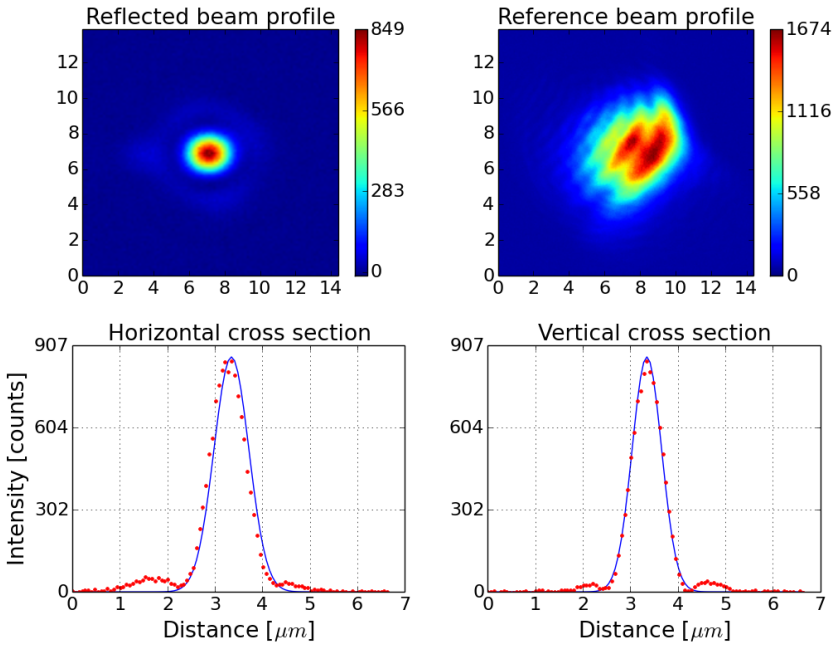

Figure 3.3: In the top two images, beam profiles as captured by the CCD are shown. On the axes is the distance in μm. In the bottom two graphs, cross sections of the reflected beam profile (red dots) and their Gaussian fits (blue line) are shown. The considered sample is ZAP1.

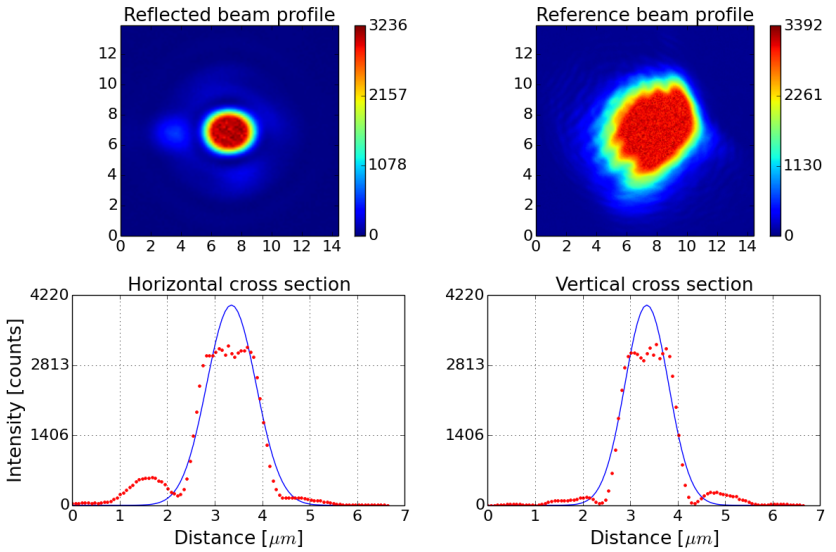

Figure 3.4: Saturated beam profiles and attempted fits. In the top two plots, all axes display the distance in μm. Note also the appearance of an extra peak left of the reflected beam profile.

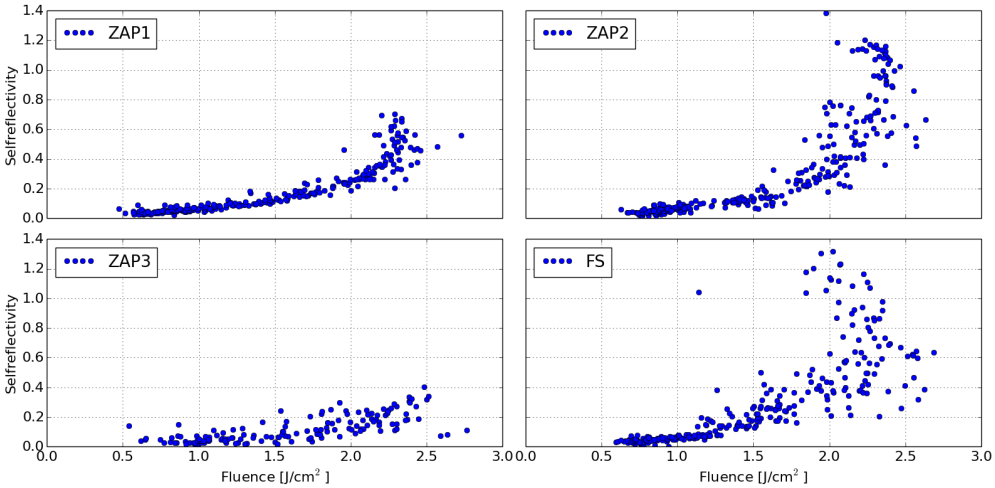

Figure 3.5: Selfreflectivity plotted against fluence for the four samples.

the experiment, saturation of the camera is prevented by checking the highest pixel value in an image. Since the camera is 12 bit, saturation is expected expected at a value nearing $2^{12} - 1 = 4095$ (before background subtraction). However, the images show saturation at a much lower value (note: the background subtraction lowers the pixel values by less then 100 ADU). Overlapping supposedly saturated peaks however, shows they all have the same pixel values. This makes it very likely that the camera is actually saturated. The same occurs for the beam profiles used in the power calibration. However, the saturation only happens when the pixelsum is larger than 2×10^7 ADU, so this doesn't fully explain the parabolic behaviour.

From the beamprofiles, the selfreflectivity is calculated as well. This is defined as the ratio between the incoming and the reflected energy ($E_{\text{inc}}$and E_{rfl} respectively) by the sample. Regardless of the nonlinear behaviour of the reference beam, the reflected beam is assumed to display a linear relation between pixelsum and energy. The selfreflectivity is then calculated by

$$R_{\text{self}} = \frac{E_{\text{rfl}}}{E_{\text{inc}}} = \frac{\text{pixelsum reflected beamprofile}}{E_{\text{inc}}} \times C_{\text{rfl}}, \tag{3.2}$$

where C_{rfl} is a calibration factor. This calibration factor is determined by having low fluence pulses result in the Fresnel reflectivity, calculated using the refractive indices in Table 3.1. Excluding the beamprofiles which saturated the camera, the resulting (fluence, selfreflectivity)-plots are shown in Fig. 3.5.

For increasing fluence, higher selfreflectivities are observed. Note however that there are datapoints with impossibly high selfreflectivities (i.e. > 1). The calculated fluences are also very low, and the change in reflectivity at these low fluences is not predicted to happen to high band gap materials by other authors[16, 26]. From this, it

can only be concluded that the calibration of the pulse energy with the reference beam failed, either due to a broken power meter or incorrect allignment of the reference beam (which seems to be clipped). Furthermore there is much more spread in the data at high fluences. This may be caused by the spacing between two consecutive shots. If a crater is ablated at the surface, debris will scatter around it. If the spacing is too smal, this debris will land and shot at by the following laser pulse.

3.4 Results: nanocraters

Using Atomic Force Microscopy (AFM), the sample's surfaces are observed. As an example, Fig. 3.6 shows the crater array of ZAP1. In these figures, every column is produced with the same laser energy (up to non-neglible pulse-to-pulse variations). The highest energy craters are near $x = 0\,\mu$m, the lowest energy craters that still fitted within this AFM field are near $x = 95\,\mu$m. It can be seen that higher energy pulses lead to deeper craters (as expected), but that there are still big variations in the crater depth for a single pulse energy. The bottom image in Fig. 3.6 seems to suggest that there may be regions on the glass itself that are more or less suitable for crater fabrication. Compare for instance the top half to the bottom half of the image.

In Fig. 3.7, the horizontal and vertical cross section of one crater are shown. A structure resembling a rimmed crater can be seen, which was also found for the semiconductor silicon by Zhang[6]. Sub-micron sized craters are found with high aspect ratios, such as for the crater shown in Fig. 3.7, $\frac{\text{diameter}}{\text{depth}} \approx \frac{845\,\text{nm}}{69\,\text{nm}} \approx 12$. The craters are wider than they are deep, contrary to what the aspect ratio in Fig. 3.7 suggests.

As is done in[6], the craters are tried to fit to

$$\begin{aligned} Z(x,y) = &-B\exp\left\{-\left[\frac{(x-x_{\text{crater}})^2}{w_{\text{crater,x}}^2}+\frac{(y-y_{\text{crater}})^2}{w_{\text{crater,y}}^2}\right]\right\}+B \\ &+A\exp\left\{-\left[\sqrt{\frac{(x-x_{\text{rim}})^2}{w_{\text{rim}}^2}+\frac{(y-y_{\text{rim}})^2}{w_{\text{rim}}^2}}-\frac{\Delta d}{w_{\text{rim}}}\right]^2\right\} \\ &-A\exp\left\{-\left[\frac{\Delta d}{w_{\text{rim}}}\right]^2\right\}. \end{aligned} \tag{3.3}$$

In this form, the bottom of the crater is defined at $Z = 0$ and the depth of the crater is parameterised by B. For the crater in Fig. 3.7, the data is fitted reasonably well. Especially in the horizontal direction (which coincides with the direction of movement of the AFM tip), there is good agreement. However, not all craters were smooth enough to fit to Eq. 3.3. The rough surface and overall noisy data also support the hypothesis that there may have been debris in the way. This makes

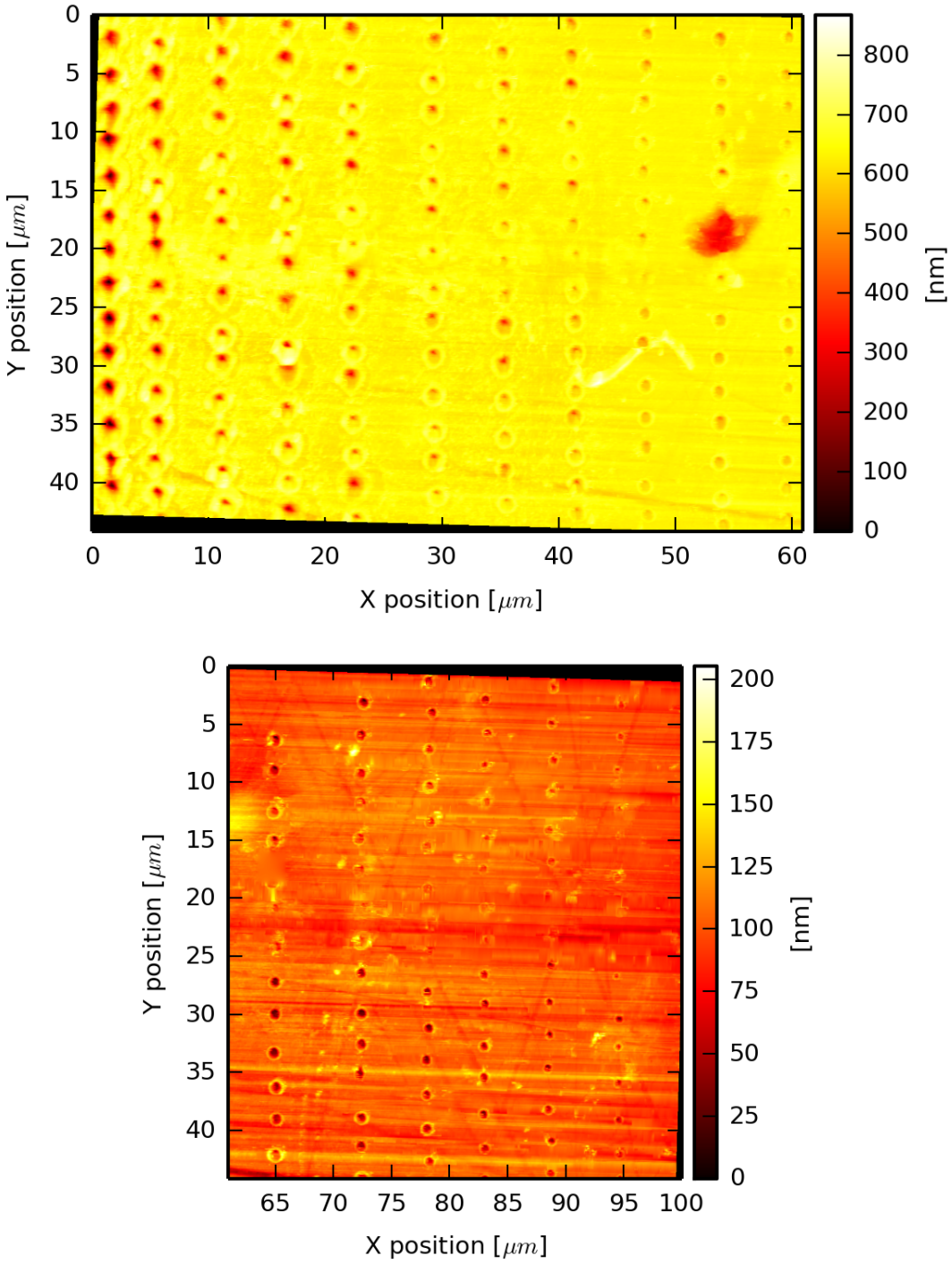

Figure 3.6: Nanocrater arrays of ZAP1. These are two parts of the same AFM image, but the original is split up to increase contrast. The direction of movement of the AFM tip is approximately horizontal. Note the difference in colorbars.

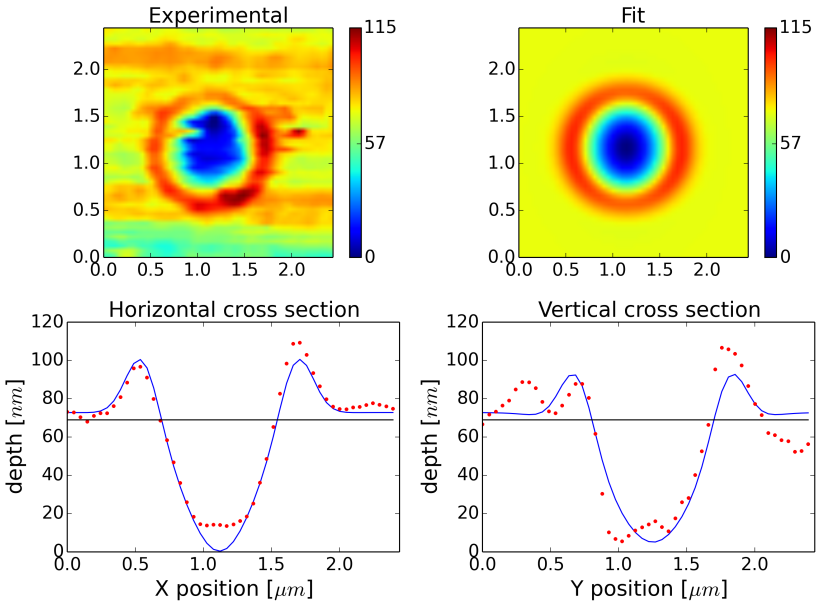

Figure 3.7: Cross sections and fit of the crater at position $(41\,\mu\mathrm{m}, 34\,\mu\mathrm{m})$. In the top two plots, the axes show distance in in μm and the colorbar shows depth in nm. In the bottom two plots, the black line indicates the average local height of the glass.

it difficult to make more quantitative statements about the crater shapes for now. Instead, the crater depth is defined in the following way. The local height of the glass is defined as the average of the outermost 12 nm (or 5 datapoints) of the square region in which a crater lies (50x50 datapoints). From this average, the minimum value of the square region is subtracted. This defines the depth of the crater. The crater depths, for all four samples, are plotted in Fig. 3.8 as a function of fluence. Because of camera saturation, there is no information about the beamwaists for high energy pulses. There is however information about the pulse energy, since the energy calibration was performed with the same saturation. Therefore it is chosen to calculate the fluence for high energy pulses using the average effective area. As expected, the depth of ablated craters increases with fluence. In this fluence range the increase in depth seems exponential with fluence for the ZAP glasses. The ZAP glasses allow for greater craters than fused silica, which is to be expected from their respective band gaps.

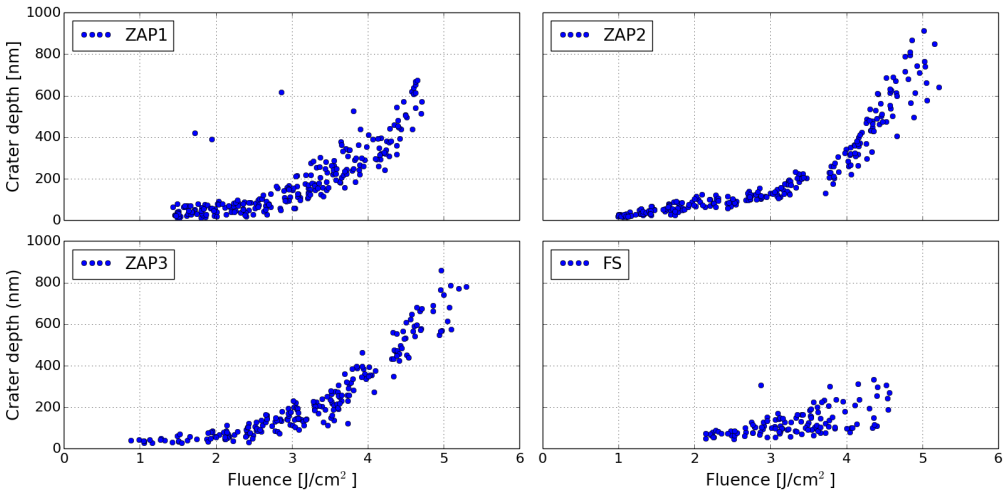

Figure 3.8: Crater depth plotted against pulse energy for the four samples.

3.5 Conclusions and outlook

This experiment shows craters with high aspect ratios can be produced using single shot femtosecond laser ablation, with various depths. It can be concluded that both the selfreflectivity and the crater depth increase with fluence. Even though more of the incoming laser pulse is reflected by the surface plasma, the laser's energy penetrates deeper into to surface for higher fluence. In order to make more quantative statements about the selfreflectivity and crater morphology, the experiment needs to be redone with the following considerations in mind. First of all, a proper energy calibration needs to be performed. Secondly, camera saturation must be avoided, preferably by using a camera that does not saturate at $\sim 80\%$ of its maximum pixel intensity. Thirdly, the correct fluence range needs to be studied. For instance, at very high fluences the plasma will have reached its maximum electron density. Here it is expected that the reflectivity will drop due to electron heating. Similarly, it would be interesting to study how deep ablated craters can get. Finally, the flatness and purity of the glass surfaces should be ensured. For this the spacing between adjecent craters needs to be sufficiently big so that no debris ends up at possible crater locations.

4 Reflectivity under weak focussing conditions

After studying the laser's self-action through selfreflectivity, there are still questions about the energy coupling into glasses. In the previous chapter our experiment provided information about the time-integrated, partially reflected laser pulse, which means it did not provide information about the *dynamics* of the laser-matter interaction. In order to study the dynamical interaction between femtosecond laser pulses and glass a different type of experiment needs to be performed. A setup with a pump beam to interact with the glass, and a probe beam to act as a camera flash and illuminate the glass surface is used. By varying the temporal delay between the pump and probe beam, the dynamics of the resulting plasma can be studied. This pump-probe setup was realized at UC Davis in California, and is shown in Fig. 4.1. This setup allows for imaging the surface plasma of the glass as a function of the delay time of the probe beam. In this experiment, only fused silica (FS, see Table 3.1) was studied.

4.1 Pump probe setup

A Titanium Saphire laser amplifier (Spitfire LCX, Spectra Physics) delivers 800 nm pulses with Gaussian temporal and spatial profiles (with a nominal pulse duration of 150 fs (FWHM) and maximum pulse energy of 250 μJ). A pulse passes a mechanical shutter (MS, Uniblitz), a zero order lambda half-wave plate ($\lambda/2$), and a polarizing beamsplitter cube (PBS). Here the pulse is divided in a pump and a probe pulse. The pump pulse passes an apperture with a diameter of 7.5 mm, then another $\lambda/2$ and PBS where its energy can be controlled, and is lastly loosely focussed onto the glass sample's surface. A lens with a focal distance of 200 mm is used, in contrast to the strongly focussing microscope objective used in the previous experiment. Due to the weak focussing, the submicron sized features from before are no longer obtained. However, the physics involved in weak-focussing conditions is much less complex and easier to interpret. The beam impinges on the sample at an angle of roughly 55°, so that it reflects away from the nearby microscope objective (MO). This pump beam is the highly energetic beam that interacts strongly with the glass. The probe beam however is made sufficiently weak in order to have negligible interaction with the glass. After the PBS it is guided through a temporal delay line. Here it can be tuned to arrive at the sample at a different time than the pump beam. The delay line consists of a retroreflector, whichs reflects a beam at exactly 180° with a slight offset in position. This retroreflector is mounted on a linear motor stage, where it can move in steps of 7 μm, which corresponds to 46 fs. After the delay line, the probe beam passes through a telescope with a barium borate crystal (BBO) in its center. This BBO crystal frequency-doubles the laser pulse from the infrared to the visible blue (400 nm). Next it is filtered by a blue filter to reduce any infrared light still present. After the telescope, the now blue pulse is guided to the sample by

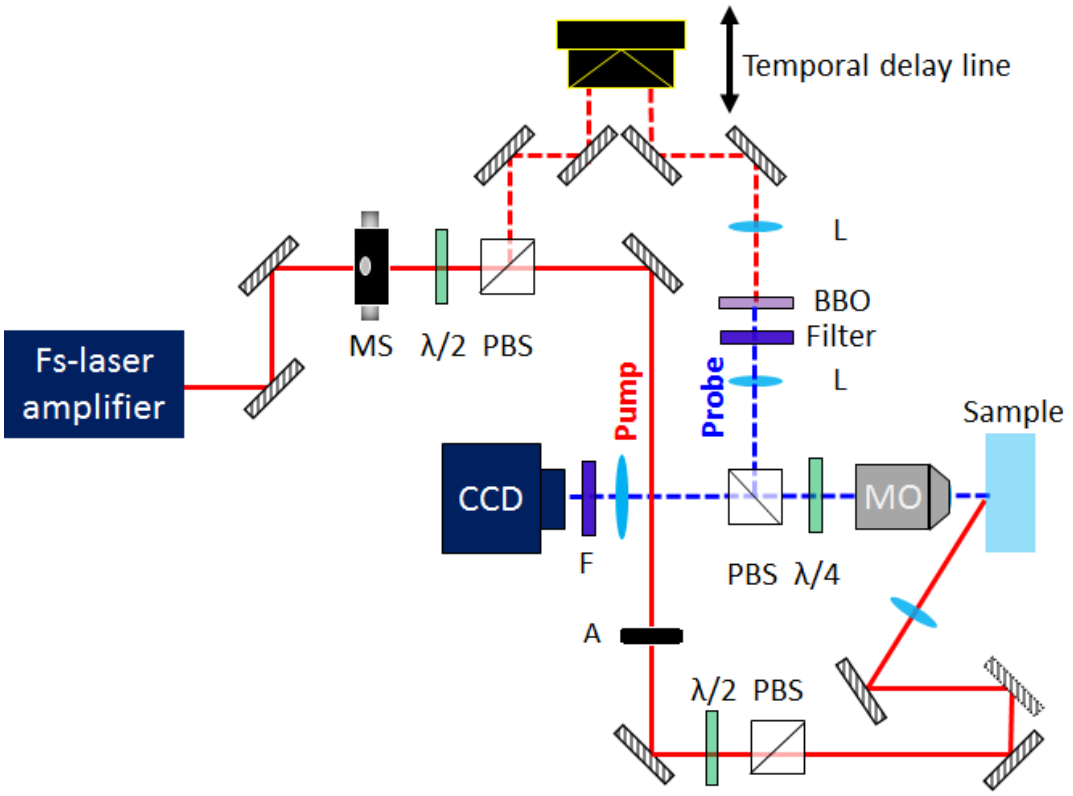

Figure 4.1: Pump-probe setup, namely the fs microscope, for studying transient reflectivity. Again, dashed rectangles represent mirrors and blue ovals represent lenses.

another PBS, through a lambda quarter-wave plate ($\lambda/4$). This waveplate circularly polarizes the light, which then passes through an MO (Mitutoyo 20x, NA=0.25) and arrives at the sample under normal incidence. Here it illuminates the plasma created by the pump beam and is reflected back through the MO, $\lambda/4$, and PBS. The lambda quarter-wave plate linearly polarizes the reflected probe beam and circularly polarizes any blue light emitted by the laser-induced plasma. The PBS filters out this plasma emission while remaining the reflected probe beam. This passes a blue filter (transmission curve centered at 400 nm with a 10 nm FWHM) to surpress white light emitted by the plasma. Finally, this light is focussed onto a triggered CCD camera (PCO Pixelfly).

With this femtosecond microscope setup, the laser-induced plasma can be imaged as a function of delay time of the probe pulse. What the camera observes is a convolution of the plasma's reflectivity and the probe pulse. This allows for a dynamic study of the plasma evolution by changing the delay time. The first step in the experiment is determining the 'zero delay'. The zero delay could be defined as when the pump pulse and probe pulse arrive at the sample simultaneously. However,

determining when this happens is difficult since it does not correspond to e.g. the maximum reflected intensity. It is also practically impossible to accurately measure the exact pathlengths of both pulses. Therefore the zero delay is defined as the delay at which the probe pulse first has an increased reflectivity at the spot where the pump beam hits the glass sample. In other words, the zero delay is defined as the delay where the pump beam has significantly interacted with the glass sample.

4.2 Results: transient reflectivity of fused silica

For this experiment, the pulse duration is set to 360 fs (FWHM, as measured by a commercial single-shot autocorrelator) by detuning the compression stage of the laser amplifier. The same fused silica sample is used as in the ablation experiment (see Table 3.1). The pump pulse energy arriving at the sample is 121 μJ, resulting in a peak fluence of 21 $^{\mathrm{J}}/_{\mathrm{cm}^2}$. Fig. 4.2 shows the images as captured by the CCD camera when the probe beam is delayed by 1 ps. Shown in (a), a background image is taken before pump-beam irradiation. This only shows the glass sample surface. Next, an image is taken when the pump beam is interacting or has interacted with the glass (depending on delay time). The plasma created by the pump has a higher reflectivity, as can be clearly seen in (b). In (c), the images from (a) and (b) are divided by eachother, pixel by pixel, to normalize the amount of light captured by each pixel. The average background has a value of 1, whereas the reflective plasma has a value > 1. In order to analyze the reflectivity, the image is contracted horizontally by a factor of 1.8 (i.e. the plasma's ellipticity) using a bicubic interpolation algorithm from the image processing software ImageJ[1]. Now the ellipsoidal plasma looks circular, and its reflectivity is approximately constant for a certain distance from the center of the plasma. A radial averaging is performed[2] to obtain the reflectivity as a function of the distance to the laser spots center. Different radial positions correspond to different values of the local fluence.

[1] ImageJ 1.49p99, `http://imagej.nih.gov/ij/`

[2] Using the Radial Profile Extended plugin for Imagej, `http://rsbweb.nih.gov/ij/plugins/radial-profile-ext.html`

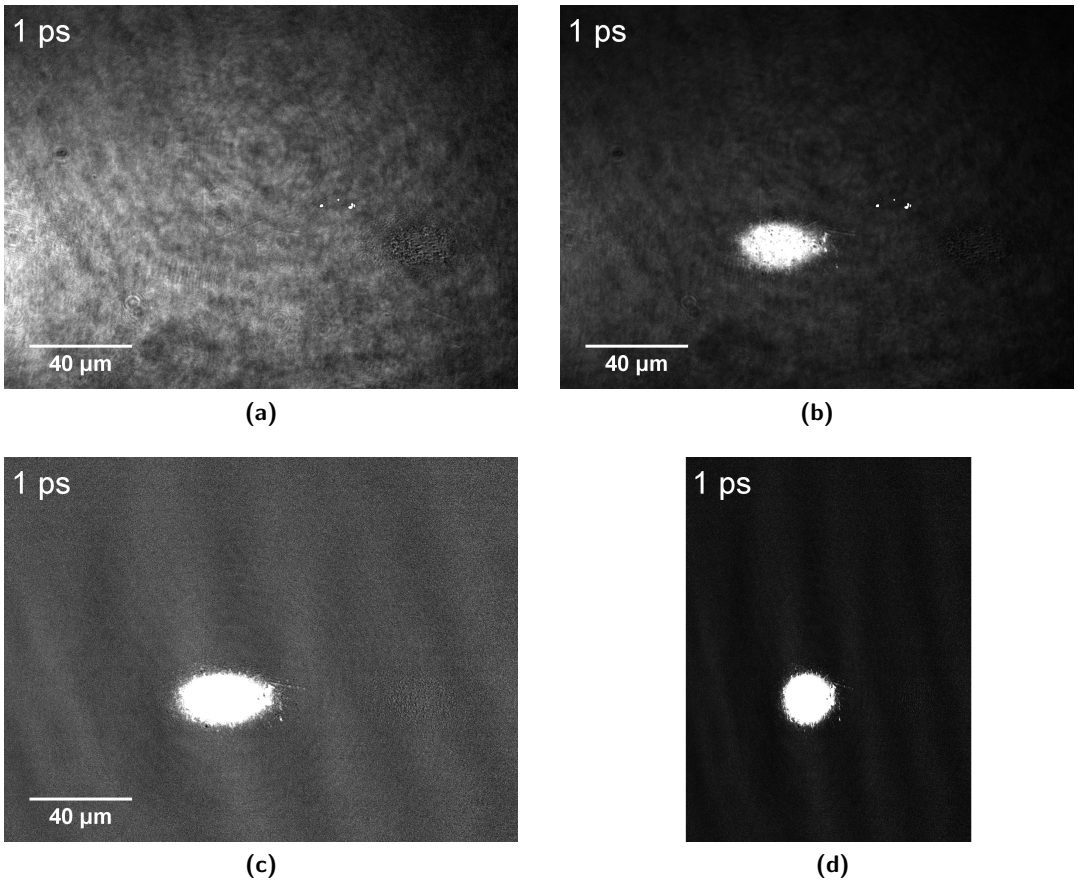

Figure 4.2: Example of an image taken with the fs microscope setup at a delay of $1\,\mathrm{ps}$, and the steps taken for data processing. The contrast varies per image for clarity, which leads to perceived saturation of some images. Also note that the camera has some dead pixels, as can be seen in (a) and (b). (a) First, a background image is taken before irradiation. (b) Secondly, the plasma illuminated by the delayed probe pulse and imaged. (c) The image in (b) is divided by the background shot from (a), pixel by pixel. (d) The normalized image of the plasma is contracted horizontally by a factor of 1.8 to obtain a radially symmetric plasma.

Before moving on to that quantative data, Fig. 4.3 shows the phases the plasma goes through during and after irradiation by the pump beam. During the first picoseconds the plasma is generated and reaches its peak density after about 1.5 ps. After this phase, the electrons in the plasma start to recombine with the glass, decreasing the reflectivity. Peculiarly though, a plasma ring remains when the bulk of the plasma has already recombined. This observation was also made by Puerto *et al.*[23] If recombination is assumed to happen, the plasma ring requires electrons from somewhere to remain more reflective than the surrounding plasma. Thus this effect may indicate the importance of electron diffusion at least at these higher timescales. Around this same time the process of ablation starts, as indicated by the debris that can be seen in the 9 ps-delay image. This debris, in the form of irregularities in the image, can be seen to be present at this specific delay, but not in the image shot after the interaction (the afterimage). In the next nanosecond, ablation occurs untill the crater finally settles in its final form. The laser creates a crater with a rim, both with a rough surface, so that the reflectivity is lowered in this region due to scattering.

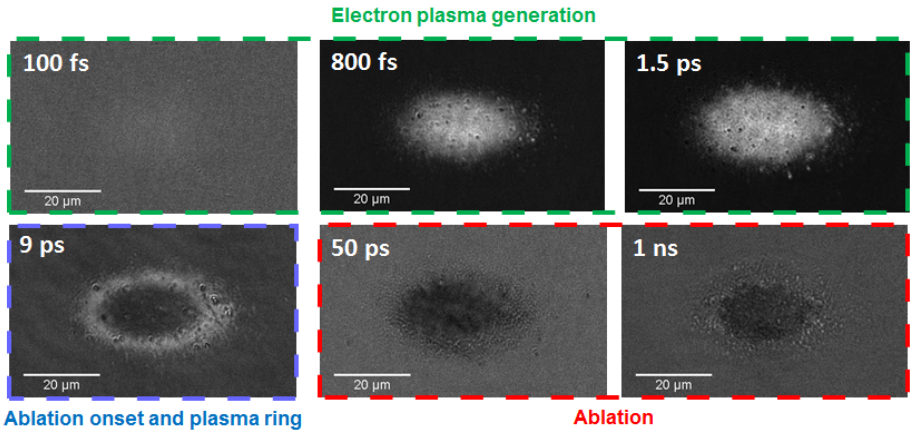

Figure 4.3: Different phases of the plasma during and after the laser-matter interaction. First electron plasma generation, which increases the reflectivity. Secondly the onset of ablation and formation of a plasma ring. Lastly ablation and the ablated crater.

In contrast to several metals[27], semiconductors[27], and other dielectrics[28], no Newton rings are observed. These Newton rings were observed in silicon and three metals in the pioneering work by Sokolowski-Tinten *et al.*[27], and indicated a liquid state of matter during short pulse laser ablation. The lack of Newton rings in this experiment with dielectrics can be attributed to the low refractive index contrast between the liquid-gaseous phase and bulk of fused silica.

Using the method explained earlier, this data is quantified for several delay times. For several radial distances from the plasma's center, the reflectivities are plotted versus probe beam delay time in Fig. 4.4. Note that the horizontal axis has a logarithmic scale, and the vertical axis is normalized to unexcited silicon. For reference, the reflectivity of unexcited silicon for 400 nm is 3.6 %. From these plots it can be seen that the plasma's risetime is about 500 fs. The reflectivity decreases after about 500 fs near the center, but only later on near the edge, after up to 2 ps. This suggests that the electrons from the center of the plasma move outward before recombining and likely later on form the observed plasma ring. After 10 ps, ablation occurs, indicated by a lower reflectivity due to scattering. Because of the rough surface of the crater, the final reflectivity is lower than 1.

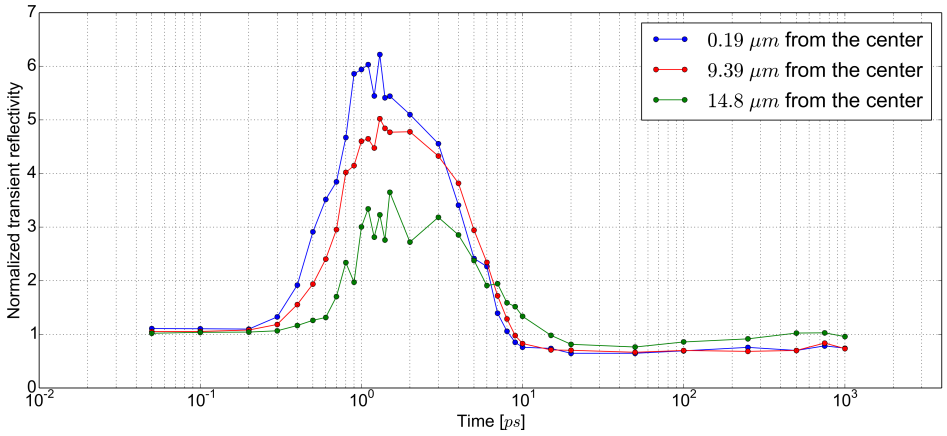

Figure 4.4: Reflectivity of the plasma as a function of probe delay time normalized to unexcited fused silica. The different plots correspond to different radial positions in the plasma. Note that $0.19\,\mu$m is practically the center of the plasma, and that $14.8\,\mu$m corresponds to the plasma ring.

4.3 Conclusions

The temporal and spatial dependence of reflectivity can be summarized in a two dimensional colormap, which is shown in Fig. 4.5. It shows the conclusions of this experiment:

- The risetime of the plasma density is about 500 fs, which is longer than the pulse duration of 360 fs (FWHM). This means that nonlinear photoionization cannot be the only reason for plasma generation, since the head and/or tail of the Gaussian laser pulse contribute as well. This suggests that avalanche ionization plays a significant role for this pulse duration and intensity.
- The lifetime of the plasma is in the order of 10 ps. The reflectivity decreases first in the center of the plasma and later at the edges, where a plasma ring can be observed. This ring remains at the same radial position. It could be that electrons from the center move outwards (instead of recombining) to form the plasma ring.
- The refractive index contrast is too low to observe Newton rings in fused silica.

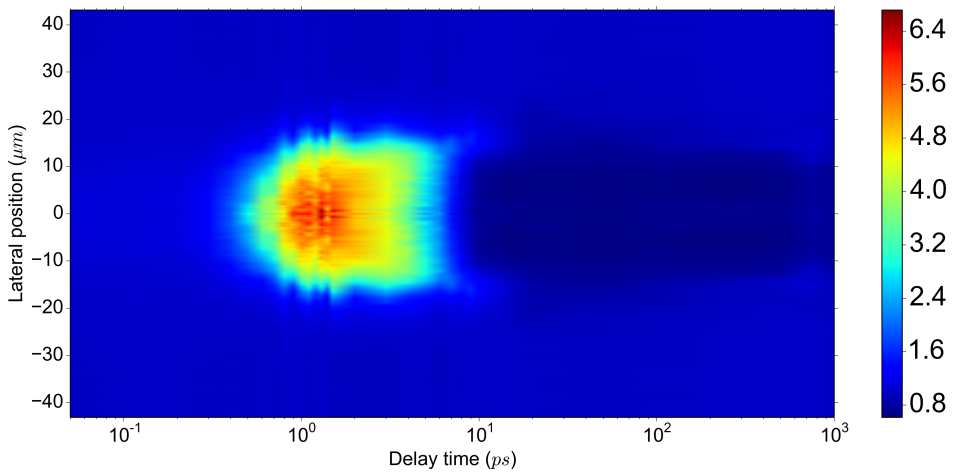

Figure 4.5: Colormap of the plasma's reflectivity. The spatial plasma evolution, peak reflectivity, rise- and lifetime of the plasma, the plasma ring, and the resulting crater can all be identified in this plot. The plot has been made symmetric around the spatial zero position for the sake of illustration.

5 FDTD simulation of the transient plasma

In the previous chapter the dynamic evolution of laser-induced plasma in fused silica was studied. In chapter 2 the theory necessary to understand this process was detailed. Using the experimental results, the theory can be tested in a simulation. In this chapter, a simulation of a fs laser pulse interacting with fused silica as in the experiment of the previous chapter is described.

5.1 The FDTD algorithm

The method used to simulate the laser-matter interaction in the experiments is the Finite-Difference Time-Domain (FDTD) method in one dimension (1D). It relies on a so-called leap frog scheme to calculate the electric and magnetic field alternatingly[29]. It is convenient to redefine the electric and displacement field according to

$$\mathbf{E} \to \sqrt{\frac{\epsilon_0}{\mu_0}}\mathbf{E}, \quad \mathbf{D} \to \frac{1}{\sqrt{\epsilon_0\mu_0}}\mathbf{D}, \tag{5.1}$$

so that their magnitudes are much closer to the magnetic and magnetizing field magnitudes, which increases numerical accuracy[30]. The 1D fields can be discretized as

$$E(z,t) \to E(k\,\Delta_z,\, n\,\Delta_t) \to E^n(k).$$

Applying the central difference approximation

$$\left.\frac{df}{dx}\right|_{x=x_0} = \frac{f(x_0 + \delta/2) - f(x_0 - \delta/2)}{\delta} \tag{5.2}$$

to Maxwell's Eqs. 2.3 and 2.4 for plane wave propagation in the z-direction, and applying the transformation from Eq. 5.1 yields

$$\frac{D_{\mathrm{x}}^{n+\frac{1}{2}}(k) - D_{\mathrm{x}}^{n-\frac{1}{2}}(k)}{\Delta_{\mathrm{t}}} = -\frac{1}{\sqrt{\epsilon_0\mu_0}}\frac{H_{\mathrm{y}}^{n}(k+\frac{1}{2}) - H_{\mathrm{y}}^{n}(k-\frac{1}{2})}{\Delta_{\mathrm{z}}} \tag{5.3}$$

and

$$\frac{H_{\mathrm{y}}^{n+1}(k+\frac{1}{2}) - H_{\mathrm{y}}^{n}(k+\frac{1}{2})}{\Delta_{\mathrm{t}}} = -\frac{1}{\sqrt{\epsilon_0\mu_0}}\frac{E_{\mathrm{x}}^{n+\frac{1}{2}}(k+1) - E_{\mathrm{x}}^{n+\frac{1}{2}}(k)}{\Delta_{\mathrm{z}}}. \tag{5.4}$$

Here Δ_{t} and Δ_{z} denote the temporal and spatial stepsizes, respectively. These equations can be rearranged into two explicit iterative equations

$$D_{\mathrm{x}}^{n+\frac{1}{2}}(k) = D_{\mathrm{x}}^{n-\frac{1}{2}}(k) - \frac{1}{\sqrt{\epsilon_0\mu_0}}\frac{\Delta_{\mathrm{t}}}{\Delta_{\mathrm{z}}}\left[H_{\mathrm{y}}^{n}(k+\frac{1}{2}) - H_{\mathrm{y}}^{n}(k-\frac{1}{2})\right] \tag{5.5}$$

and

$$H_{\mathrm{y}}^{n+1}(k+\frac{1}{2}) = H_{\mathrm{y}}^{n}(k+\frac{1}{2}) - \frac{1}{\sqrt{\epsilon_0\mu_0}}\frac{\Delta_{\mathrm{t}}}{\Delta_{\mathrm{z}}}\left[E_{\mathrm{x}}^{n+\frac{1}{2}}(k+1) - E_{\mathrm{x}}^{n+\frac{1}{2}}(k)\right]. \tag{5.6}$$

As can be seen from the offset of $\frac{1}{2}$ in the indici k and n between the two equations, a discretization like this leaves the spacetime grid for the D- and E-fields interweaved with the spacetime grid for the H-and B-fields. The two type of fields are offset by half a stepsize, both spatially and temporally, with respect to eachother. Another important fact is that the future D-field depends on its past value and the values of the H-fields on the gridpoints closest to it in space. The dependence of the future H-field on the past H-field and adjacent E-fields is completely analogous. The relation connecting Eq. 5.5 to Eq. 5.6 is given by[8]

$$D(\omega) = \epsilon(\omega)E(\omega), \tag{5.7}$$

where $\epsilon(\omega)$ denotes the relative dielectric function, and the fields are already transformed according to Eq. 5.1. With this set of equations and a source term to simulate the laser pulse, the propagation of the electromagnetic wave can be described.

5.2 The dielectric response and reflectivity

In the experiments, the laser changes many of the glass' optical properties. Every one of these changes is governed by the dielectric function, and hence Eq. 5.7 is the only equation needed to incorporate the effects of the laser on the glass. This equation, however, is formulated in the frequency domain whereas Eq. 5.5 and Eq. 5.6 are formulated in the time domain. In order to apply Eq. 5.7 in the time domain, it has to be Fourier transformed. First the dielectric function 2.7 is expressed in the Debye form as

$$\epsilon(\omega) = (n_0 + n_2 I)^2 - \frac{\sigma_{\mathrm{Drude}}}{i\omega} + \frac{\chi}{1 - i\omega\tau}, \tag{5.8}$$

where $\sigma_{\mathrm{Drude}} = \epsilon_0\omega_{\mathrm{p}}^2\tau$ is the Drude model conductivity, $\chi = -\omega_{\mathrm{p}}^2\tau^2$ is the Debeye dispersion term, and $\omega_{\mathrm{p}}^2 = \frac{\rho e}{m_{\mathrm{eff}}\epsilon_0}$ is the plasma frequency. In this form the effects of conductivity and dispersion in general on the electric field are clearer. Using the

convolution theorem, Eq. 5.7 can be inverse-Fourier transformed as

$$\begin{aligned}
\mathcal{F}^{-1}\{D(\omega)\} &= \mathcal{F}^{-1}\left\{\left[(n_0+n_2 I)^2 - \frac{\sigma_{\text{Drude}}}{i\omega\epsilon_0} + \frac{\chi}{1-i\omega\tau}\right]E(\omega)\right\} \\
D(t) &= (n_0+n_2 I)^2\,\mathcal{F}^{-1}\{E(\omega)\} - \frac{\sigma_{\text{Drude}}}{\epsilon_0}\mathcal{F}^{-1}\left\{\frac{1}{i\omega}E(\omega)\right\} \\
&\quad +\chi\mathcal{F}^{-1}\left\{\frac{1}{(1-i\omega\tau)}E(\omega)\right\} \\
&= (n_0+n_2 I)^2\,E(t) - \frac{\sigma_{\text{Drude}}}{\epsilon_0}\mathcal{F}^{-1}\left\{\frac{1}{i\omega}\right\} * \mathcal{F}^{-1}\{E(\omega)\} \\
&\quad +\chi\mathcal{F}^{-1}\left\{\frac{1}{1-i\omega\tau}\right\} * \mathcal{F}^{-1}\{E(\omega)\} \qquad (5.9)
\end{aligned}$$

Here the two convolutions, denoted by a $*$, are calculated as

$$\begin{aligned}
\mathcal{F}^{-1}\left\{\frac{1}{i\omega}\right\} * \mathcal{F}^{-1}\{E(\omega)\} &= -\text{sgn}(t) * E(t) \\
&= -\int_0^t E(t')dt' \qquad (5.10)
\end{aligned}$$

and

$$\begin{aligned}
\mathcal{F}^{-1}\left\{\frac{1}{1-i\omega\tau}\right\} * \mathcal{F}^{-1}\{E(\omega)\} &= \frac{1}{\tau}\left[e^{-\frac{|t|}{\tau}} - 1\right] * E(t) \\
&= \int_0^t e^{-\frac{t-t'}{\tau}}E(t')dt'. \qquad (5.11)
\end{aligned}$$

Eq. 5.9 can then be evaluated numerically as

$$\begin{aligned}
D(t) &= (n_0+n_2 I)^2\,E(t) + \frac{\sigma_{\text{Drude}}}{\epsilon_0}\int_0^t E(t')dt' + \frac{\chi}{\tau}\int_0^t e^{-\frac{t-t'}{\tau}}E(t')dt' \\
D^n &= (n_0+n_2 I)^2\,E^n + \frac{\sigma_{Drude}}{\epsilon_0}\sum_{i=0}^{n} E^i\Delta_t + \frac{\chi}{\tau}\sum_{i=0}^{n} e^{-\frac{\Delta_t}{\tau}(n-i)}E^i\Delta_t. \qquad (5.12)
\end{aligned}$$

In order to obtain an expression for the new value of the E-field Eq. 5.12 needs to be solved for E^n. This results in

$$E^n = \frac{D^n - \frac{\sigma_{\text{Drude}}}{\epsilon_0}\Delta_t\sum_{i=0}^{n-1}E^i - \frac{\chi}{\tau}\Delta_t\sum_{i=0}^{n-1}e^{-\frac{\Delta_t}{\tau}(n-i)}E^i}{(n_0+n_2 I)^2 + \frac{\sigma_{\text{Drude}}}{\epsilon_0}\Delta_t + \frac{\chi}{\tau}\Delta_t}. \qquad (5.13)$$

Note that the new value for the E-field depends on the new value for the D-field and all previous values of the E-field.

In this form, only the Drude model is taken into account. The effects of strong field ionization have not been accounted for yet. Clearly, the incoming wave should attenuate even more due to SFI because this process takes energy out of the wave. Consider a Lambert-Beer-like law for the attenuation of intensity inside a material[31]

$$\frac{dI}{dz} = -\alpha(I)I(z), \tag{5.14}$$

where $\alpha(I)$ the inverse penetration depth. This means the intensity approximately scales according to $I \propto \exp(-\alpha(I)z)$. The validity of this approximation is discussed in appendix B. Within the same approximation, intensity scales according to $I \propto \exp(-2\mathrm{Im}(n)k_0 z)$, with k_0 the wavenumber of the incoming wave in vacuum. Now both formulas can be equated and the inverse penetration depth can be identified as

$$\alpha(I) = 2\mathrm{Im}(n)k_0. \tag{5.15}$$

The imaginary part of the refractive index $\mathrm{Im}(n)$ relates to the imaginary part of the dielectric function via $\mathrm{Im}(\epsilon) = 2\mathrm{Re}(n)\mathrm{Im}(n)$. In turn, the imaginary part of the dielectric function relates to the conductivity via $\mathrm{Im}(\epsilon) = \frac{\sigma}{\omega\epsilon_0}$. Conclusively, the conductivity due to SFI is

$$\sigma_{\mathrm{SFI}} = \mathrm{Re}(n)\epsilon_0 c\alpha(I). \tag{5.16}$$

On the other hand, we can use the continuity equation[32]

$$\frac{d\Omega}{dt} + \frac{dI}{dz} = 0, \tag{5.17}$$

where Ω is the energy density, to find an expression for $\alpha(I)$. The time derivative of the energy density is nothing more the rate of electrons being ionized, times the energy per electron. Hence $\frac{d\Omega}{dt} = U_{\mathrm{eff}} W_{\mathrm{SFI}} \left(1 - \frac{\rho}{\rho_{\max}}\right)$. Solving then the continuity equation for $\alpha(I)$, and plugging in results in $I = \frac{1}{2}\mathrm{Re}(n)\epsilon c|E|^2$, results in

$$\alpha(I) = \frac{2U_{\mathrm{eff}} W_{\mathrm{SFI}} \left(1 - \frac{\rho}{\rho_{\max}}\right)}{\mathrm{Re}(n)\epsilon_0 c|E|^2}. \tag{5.18}$$

Our final expression for the conductivity of the glass due to SFI is

$$\sigma_{\mathrm{SFI}} = \frac{2U_{\mathrm{eff}} W_{\mathrm{SFI}} \left(1 - \frac{\rho}{\rho_{\max}}\right)}{|E|^2}. \tag{5.19}$$

Now field attenuation as a result of SFI can be accounted for by changing σ_{Drude} in Eq. 5.13 to $\sigma_{\mathrm{Drude}} + \sigma_{\mathrm{SFI}}$.

Using Eqs. 5.5, 5.6, and 5.13 the propagation of all fields can be calculated. The corresponding intensity is calculated using $I = \frac{1}{2}n\epsilon c|E|^2$. Note that this implies that when E is time-dependent, so is I. This would drastically complicate the inverse

Fourier transform in Eq. 5.9 and the explicit calculation of E^n in Eq. 5.13. Therefore the slowly varying envelope approximation is applied, which assumes that the electric field amplitude does not change much on small time scales. In this case, it is taken to be constant over the duration of half a wave, so that Eq. 5.13 is still correct. How the amplitude (and phase) of the electric field can be extracted from the electric field during half a wave is explained in appendix C.

After the simulation has propagated all fields through the simulation space and time, the reflectivity can be extracted from this data. This is done using the Poynting vector $S = \mathrm{Re}\left(E_\mathrm{x} H_\mathrm{y}^*\right)$ (which is scalar for a planar wave in one dimension), where * denotes a complex conjugate. A certain point in the simulation space acts as a detector point. By integrating the Poynting vector at this point over time, the energy passing this point is found. The simulation is run twice, once in the absence of any material (so just a wave in vacuum) and once in the presence of the glass. The energy directed to the glass can be calculated by integrating S over the duration of the simulation. To calculate the energy reflecting off the surface, the fields that are reflected need to be known. They can be calculated by subtracting the incoming fields (E_inc, H_inc, obtained from the simulation in absence of glass) from the total fields (E_tot, H_tot, obtained from the simulation in presence of glass). The energy reflected of the surface can then be calculated by integrating the accompanying Poynting vector at the detector plane. The reflectivity R can then be calculated as the ratio of the reflected energy to the incoming energy at the detector point

$$R = \frac{\int S_\mathrm{out}(x_\mathrm{detector})dt}{\int S_\mathrm{inc}(x_\mathrm{detector})dt} \cong \frac{\sum_n \mathrm{Re}\left[\left(E_\mathrm{tot}^n - E_\mathrm{inc}^n\right)\left(H_\mathrm{tot}^{n*} - H_\mathrm{inc}^{n*}\right)\right]}{\sum_n \mathrm{Re}\left[E_\mathrm{tot}^n H_\mathrm{tot}^{n*}\right]}, \tag{5.20}$$

where the integration and summation are limited by the simulation duration.

5.3 Simulating the pump probe experiment

The FDTD algorithm now allows for simulating both the pump and the probe pulse from the experiment. The simulation for the pump pulse works of course with a 1D temporally Gaussian pulse with a duration of 360 fs (FWHM) and wavelength of 800 nm. It affects the glass by increasing its free electron density according to Eq. 2.17, and therefore changes its dielectric function according to Eq. 2.7. This interaction is calculated once every half optical period, since the intensity is only properly defined after one such duration. The very similar simulation for the probe pulse also starts with a 1D temporally Gaussian pulse with a duration of 360 fs, but a wavelength of 400 nm. To compensate for the zero delay position from the experiment, it is given a (somewhat arbitrary) temporal offset of 2 pulsedurations with respect to the pump pulse simulation. On top of this, it is delayed by whichever temporal delay is beying simulated. The probe pulse does not affect the material, but instead uses the properties of the material as calculated by the pump simulation. Fig. 5.1 shows the course of the simulations schematically.

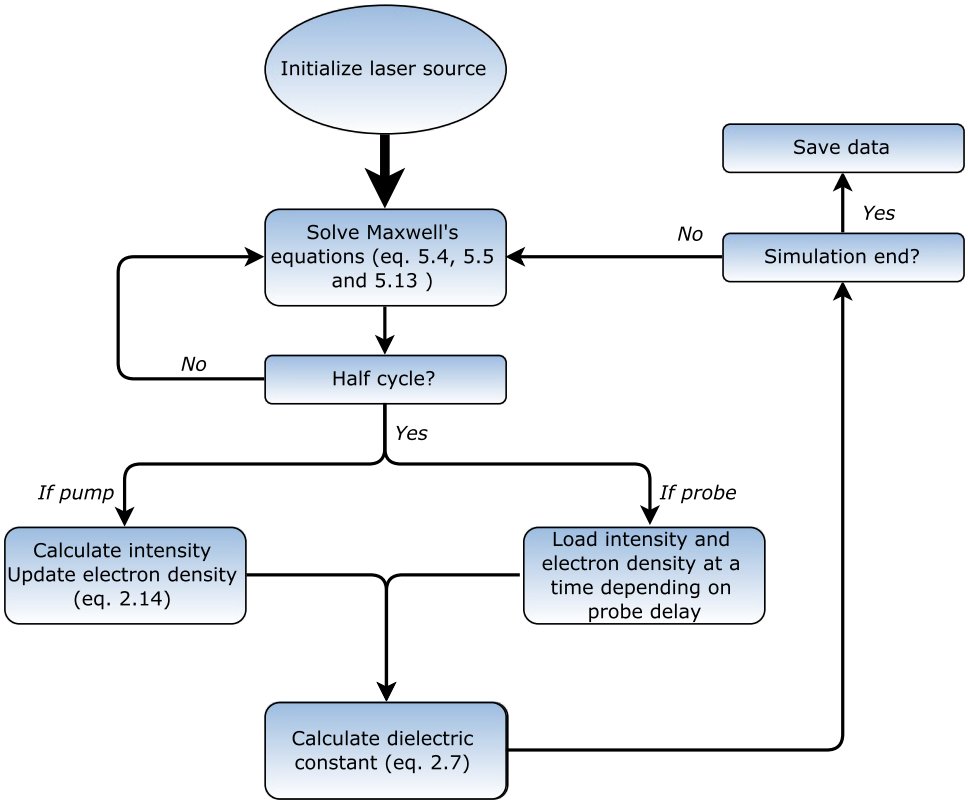

Figure 5.1: Flowchart of both the pump and probe simulation.

With all the basics of FDTD theory outlined, the simulation space can be formed. In order to safe time, and since the experiment was performed in weak focussing conditions, a one dimensional space is used. It consists of a small vacuum region where the source will be modeled, and a region with the properties of the glass. The finite simulation space needs to be terminated, which is not as straightforward as it may seem. If, for instance, at the edge of the simulation space the electric field is defined to be zero, the edge will be no different than a perfect conductor. The electromagnetic wave will see the edge of the simulation as a perfectly conducting metal wall and completely reflect back. A more effective simulation boundary would not reflect any part of the wave, but negate it completely. The way this is done in this simulation is by formulating a perfectly matched layer (PML). PMLs do not reflect any part of the wave, but do make it decay. Therefore at the end of the PML, only a small part of the wave is reflected back. Because the decay of the PML is big enough, this reflected part will have a neglegible effect on the simulation. For more details about PMLs, see Sullivan[30] or Schneider[33]. A PML with a thickness of about two times the wavelength is used. The simulation space is shown schematically in Fig. 5.2. The next step in designing the simulation space is determining suitable spatial and temporal stepsizes. A necessary (but not sufficient) condition for the

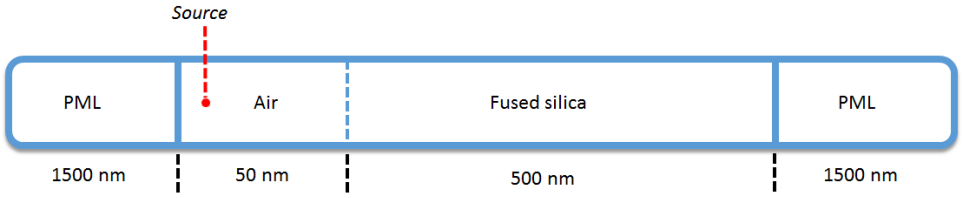

Figure 5.2: Simulation space with the location of the laser source. The distances displayed are *not* to scale.

$\mathbf{\Delta_z}$ [nm]	2	5	10	20	40	80
Reflectivity [fraction of $\mathbf{r_0}$]	0.996	1.00	1.00	1.01	1.05	1.23

Table 5.1: Simulation results for the reflectivity of ordinary fused silica (in the absence of plasma formation).

stability of an FDTD simulation is the Courant condition[33]. This condition states that the Courant number S_c , in one dimension, should obey the relation

$$S_c = \frac{c\Delta_t}{\Delta_z} < 1. \tag{5.21}$$

For this work the typical value of $S_c = 0.5$ is chosen. The spatial stepsize is determined by considering the reflectivity of unexcited fused silica, r_0. This can be theoretically calculated with Eq. 2.18 which gives $r_0 = 0.034$ for 800 nm light. For several stepsizes and an abundantly large PML (as to negate the effect of reflections off the simulation boundary for sure), the reflectivity of ordinary fused silica is calculated with the simulation. The results are shown in Table 5.1. Using Table 5.1, a spatial stepsize of $\Delta_z = 10\,\text{nm}$ is chosen. This corresponds to a temporal stepsize of $\Delta_t = 0.017\,\text{fs}$. Now the PML size can be determined. The PML size determines how much a wave decays in the PML, and thus how much is reflected off of the simulation boundary. Table 5.2 shows the dependence of reflectivity on PML size, and it tells us that a PML of 150 points is the smallest number that still gives very accurate results.

PML [gridpoints]	10	100	150	200	250	300
Reflectivity [fraction of $\mathbf{r_0}$]	2.75	0.967	1.00	1.00	1.00	1.00

Table 5.2: Simulation results for the reflectivity of ordinary fused silica (in the absence of plasma formation).

5.4 Results and discussion

The simulation is now ready to test whether the Drude model (Eq. 2.7) in combination with the single rate equation

$$\frac{d\rho}{dt} = (W_{\mathrm{SFI}} + \beta I \rho)\left(1 - \frac{\rho}{\rho_{\mathrm{max}}}\right) - \frac{\rho}{\tau_{\mathrm{s}}} \tag{5.22}$$

accurately predicts the plasma reflectivies that are observed. First the parameters of these equations have to be chosen. Values for both refractive indices are well-known, namely $n_0 = 1.4533$[25] for infrared light, $n_0 = 1.4701$[25] for blue light, and $n_2 = 3.54 \times 10^{-20}\,\mathrm{m^2/W}$[14]. There exists a bigger discrepancy in literature for the values of the effective mass of an electron m_{eff}, and for lack of a better alternative it is taken to be $m_{\mathrm{eff}} = 1\,\mathrm{m_e}$, as is often done in fused silica simulations[13,17–19,34]. Similarly, the value for the electron scattering time τ is not well-known. In this work it is taken to be constant, which means that it is effectively a pulse-averaged value. This makes it rather sensitive to the exact experimental conditions. For this reason, several different values are tested.

Now, consider the influence of the scattering time on reflectivity theoretically. For the three tested scattering times, the reflectivity is calculated as a function of density using Eq. 2.18. The resulting curves are plotted in Fig. 5.3. For low free electron densities and high enough scattering times, the reflectivity decreases. Then as the density increases, reflectivity increases, and moreso for high scattering times. A high scattering time results in almost steplike behaviour of the reflectivity. For the simulation, this would require very accurate predictions of free electron densities in order to get correct results. In the single rate equation that is employed, the avalanche ionization coefficient β is calculated by the Joule heating equation and Eq. 2.14. Four different values for the maximum allowed plasma density are also tested. Namely $\rho_{\mathrm{max}} = 5.0 \times 10^{29}\,\mathrm{m^{-3}}$, corresponding to the electron density where all electrons with an ionization potential $< 500\,\mathrm{eV}$ are ionized[21], $\rho_{\mathrm{max}} = 6.6 \times 10^{28}\,\mathrm{m^{-3}}$, corresponding to the electron density where one electron per atom is ionized, $\rho_{\mathrm{max}} = 2.2 \times 10^{28}\,\mathrm{m^{-3}}$, where one electron per molecule is ionized. The case without plasma saturation (or an infinite maximum density) is also considered. Lastly, the recombination term $-\frac{\rho}{\tau_{\mathrm{s}}}$ is neglected, since no decrease in electron density is observed in the experimentally observed plasma for the first 1.5 ps. For several combinations of these initial parameters, the simulation is run. Table 5.3 shows the maximum density reached during each of these simulations.

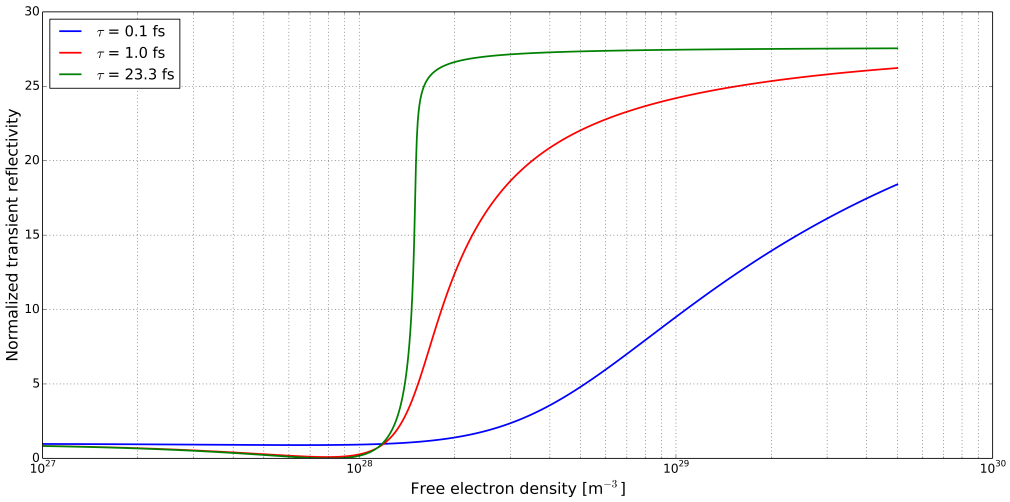

Figure 5.3: Influence of scattering time on reflectivity, calculated with the Drude model and the Fresnel equation.

From this table, a few things become clear. First of all, when AI is included but plasma saturation is not, the density reached can become unphyscially high. The maximum density that could possibly be reached in fused silica is $6.6 \times 10^{29}\,\mathrm{m}^{-3}$, since that is the total electron density present in the material. Not including AI however leads to a low density, which results in a decrease in reflectivity. This leads to three possibilities:

1. The scattering time is rather high. Only for $\tau = 23.3\,\mathrm{fs}$, acceptable electron densities occur. However, this requires that the densities predicted by the single rate equation will have an error margin of smaller magnitude than the width of the step of the green curve in Fig. 5.3.

2. Plasma saturation needs to be taken into account, and which for now can only be done phenomenologically, invoking unfundamental maximum densities.

3. The AI term is overestimated with this approach. Either the values for β during our experiment are much lower than predicted by Joule heating, or AI's dependency on the total free electron density (ignoring the energy distribution of these conduction band electrons) is incorrect.

Before expanding on these points, consider the transient reflectivities resulting from these simulations, and compare to the experimental data. These data are plotted in Fig. 5.4. As mentioned, only SFI results in too low electron densities and thus too low reflectivies. Modelling SFI and AI without plasma saturation results in way too high densities and reflectivies. Only when plasma saturation is taken into account values for reflectivity comparable to values found in our experiment are

ID	Rate equation	$\rho_{max}[\mathrm{m}^{-3}]$	τ[fs]	Maximum density $[m^{-3}]$
00	$\frac{d\rho}{dt} = W_{\mathrm{SFI}}$	-	$1.0^{[16,35]}$	8.51×10^{27}
01a	$\frac{d\rho}{dt} = W_{\mathrm{SFI}} + \beta I \rho$	-	$0.1^{[21,36]}$	1.36×10^{30}
01b	”	-	$1.0^{[16,35]}$	5.81×10^{29}
01c	”	-	$23.3^{[14]}$	5.08×10^{28}
02a	$\frac{d\rho}{dt} = (W_{\mathrm{SFI}} + \beta I \rho)\left(1 - \frac{\rho}{\rho_{\mathrm{max}}}\right)$	5.0×10^{29}	$1.0^{[16,35]}$	3.61×10^{29}
02b	”	6.6×10^{28}	$1.0^{[16,35]}$	6.60×10^{28}
02c	”	2.2×10^{28}	$1.0^{[16,35]}$	2.20×10^{28}
03a	”	5.0×10^{29}	$23.3^{[14]}$	4.83×10^{28}
03b	”	6.6×10^{28}	$23.3^{[14]}$	3.54×10^{28}
03c	”	2.2×10^{28}	$23.3^{[14]}$	1.98×10^{28}

Table 5.3: Maximum free electron densities reached during the simulation for different initial parameters.

obtained. However, even though the maximum reflectivities may agree, the slope of the simulated curves is much higher than of the experimental one. This suggests that the rise in free electron density is too rapid when modelled like this. The rapid rise to high free electron densities reached can be explained the following way. The AI rate in Eq. 5.22 does not take into account the energy distribution of the electrons in the conduction band. It considers all conduction band electrons for AI, instead of just the electrons which have enough energy to cross the band gap. It ignores the time that electrons at the bottom of the conduction band need to gain enough energy to collisionally excite a valance band electron. This time delay could result in less steep slopes for the transient reflectivity curves. Furthermore, the same constant value for the scattering time is used for each delay of the probe beam simulation. This scattering time depends on electron temperature, which will surely rise as the delay between pump and probe increases. Even if a constant scattering time is suitable for the pump beam simulation, this does not mean that the same scattering time applies to probe beam simulations at a different delay.

5.5 Conclusions and outlook

For the purpose of modelling the transient reflectivity of a plasma during a pump-probe experiment, the Drude model with constant scattering time in combination with the single rate equation does not correctly predict reflectivies of the plasma. The correct maximum reflectivity of the plasma could be predicted by picking suitable

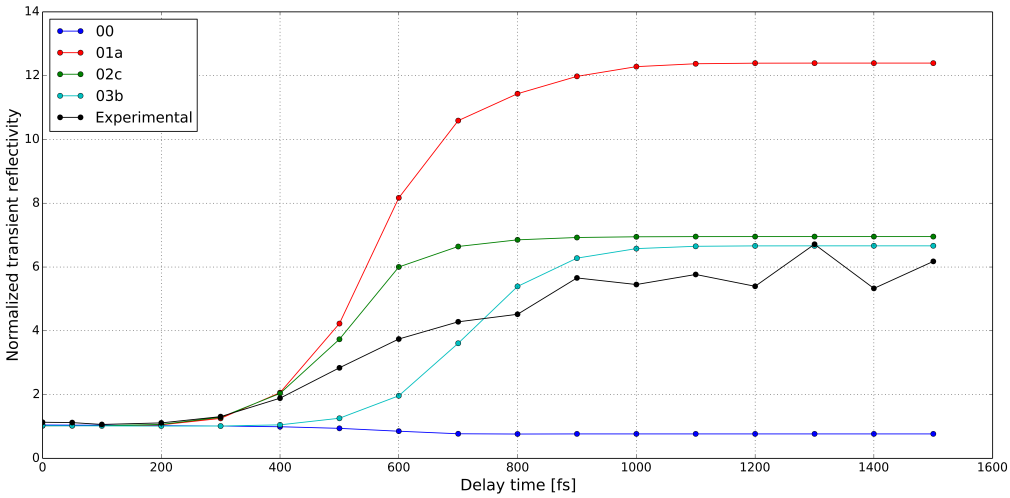

Figure 5.4: Simulated normalized transient reflectivity of the plasma for different initial parameters.

values for the scattering time and the maximum electron density, but likely more than one combination for these two parameters would suffice. Preferably, a model that takes into account (1) the free electron energy distribution and (2) a variable electron scattering time could be used.

For further research, one way to take into account the free electron energy distribution is the multiple rate equation (MRE), as developed by Rethfeld[37]. Here, the conduction band is approximated as having discrete energy levels seperated by one photon energy. Electrons at the bottom of the conduction band (getting here through SFI or AI) gain energy through one photon absorption, untill they have enough energy for collisional excitation. This model is shown to agree well with the full kinetic approach from Kaiser *et al.*[13]. It would be very interesting to see whether this model does correctly predict reflectivies. Implementing this method, in combination with a two-dimensional FDTD algorithm, would make it suitable for simulating the laser in strong focussing conditions as well.

6 Conclusions and outlook

In this work, the energy coupling of a femtosecond laser pulse into glasses is studied. In summary, the following conclusions can be drawn.

- In Section 3, the glasses' selfreflectivity and ablated nanocraters are studied. It is found that for increasing fluence, the selfreflectivity and crater depth both rise. High aspect ratio craters can be produced of various depths on all four glass surfaces.
- In Section 4, the transient reflectivity of fused silica is studied. Due to a dense electron plasma, the glass' reflectivity rises within a timespan less than 1 ps. For 360 fs pulses with a fluence of 21 $^{\mathrm{J}}/_{\mathrm{cm}^2}$, avalanche ionization is seeded by strong field ionization, in order to create the electron plasma. After several picoseconds, a plasma ring can be observed on the glass surface at a stationary position. Surface ablation sets in when the laser pulse has passed and is no longer interacting with the material.
- In Section 5, the transient reflectivity of fused silica is modelled using the Drude model with a constant scattering time, Keldysh' model for strong field ionization, and a single rate equation modelling avalanche ionization. Results of a one-dimensional finite-difference time-domain simulation do not agree with the experimentally obtained results. This disagreement is mainly due to an overestimation of avalanche ionization and the lack of an exact value for the scattering time, and potentially due to a lack of understanding of plasma saturation. The effects of the electron temperature may also be underestimated in this model.

While a qualitative understanding of the energy coupling into glass is achieved, a more quantitative understanding would be better. For this, the ablation experiment of Section 3 needs to be redone. By spacing the craters further apart no debris will occur at different craters. Likewise, use of a glass with a more homogeneous and flat surface will reduce noise in the AFM data. Quantities of interest would be depth and width of the craters as function of fluence. More control over the modification of glass may lead to technical applications.

Measurements on selfreflectivity at very high fluences, where the plasma is saturated, may indicate the roll of electron temperature. As an extension of this, the FDTD simulation can be made with a temperature-dependent scattering time. As a suggestion, the MRE by Rethfeld[37] could be used to model AI. Expanding the simulation into two dimensions, the effects of strong focussing can be accounted for. This would allow the simulation to predict results from the ablation experiment, and a relation with the ablated crater depth and width could be studied.

7 Acknowledgements

Producing a thesis has proven to be hard work. Luckily you don't have to do this kind of thing alone. Here I would like to dedicate some words to some of the people that have helped me out tremendously and that I am forever grateful to.

First of all, I would like to thank my supervisor Dries van Oosten for many things. For showing how a combination of theoretical and experimental knowledge can make for a great researcher. For always having an open door, even though there are at least four other master students, three PhD's, bachelor students and whoever else I don't even know about asking questions throughout the day. And of course for allowing me to work in his group while also being able to go to UC Davis for several months, and attending CLEO 2015 in San Jose.

For this I also would like to thank Denise Krol, who enabled my stay at her group in the department of Chemical Engineering and Materials Science at UC Davis. Working in Davis has been an incredible experience, allowing me to see and partake in physics in a different part of the world. Her guidance throughout the rest of the project is much appreciated.

Thirdly, I would like to thank Javier Hernández-Rueda. Javier has helped me since the start of this project, from teaching me how to build an experimental setup to writing a scientific thesis. I have thoroughly enjoyed our time working together in Davis and our shorter collaborations in Utrecht.

Of course you don't only learn from your supervisors, but from your peers as well. Figuring things out in the lab with nobody to tell you the correct answer can be a great teaching tool. Marcel Scholten and I endeavoured on our first laser experiment, and I would like to thank him for all his selfless help. Likewise I would like to thank Marlou Slot, for all her help with the AFM measurements. Outside the lab, having discussions with people who understand things as little as you do can lead to great aha-erlebnissen (or equally often, huh?-erlebnissen). James Findley de Regt, Marcel Scholten, Robert Schoo, Gordian Zomers, I am grateful for all the fruitful conversations we have had on the topic of ablation, or otherwise.

There are still many more people that I have worked with nearly every day, had lunch with (mostly tosti's), went to conferences with, played beerpong with, went on pubcrawls with, and so on. I would like to thank the PhD's Ole Mussman, Arjon van Lange, Sandy Pratama and Sebastiaan Greveling. I also gratefully acknowledge the other master students in the group, Anne de Beurs, Qiao Li, Karindra Perrier, Jasper Smits, Koen Sponselee, Broos Vermeulen, and Kostas Voutyras. This entire group has helped me out countless times, and has made this project a very enjoyable experience.

The technical staff of the nanophotonics group is also much appreciated. Thanks

to Frits Ditewig, Paul Jurrius, Dante Killian, and Cees de Kok, all equipment worked the way it was supposed to. I have enjoyed all the coffees, birthdaycakes, "bittergarnituur" and beverages we shared.

Finally, I would like to note that, with one rockstar, one brown belt hapkidoka, and one chilled-out-even-when-stressed Spaniard, I couldn't have wished for better supervisors. Who ever said physics is for nerds?

Appendix A Avalanche ionization through Joule heating

In this appendix an expressions for the absorbed power per unit volume of an electron gas irradiated by a laser will be derived. This absorbed power relates directly to the avalanche ionization rate.

Consider a free electron gas in an electromagnetic field. The Lorentz force

$$\boldsymbol{F} = q\left(\boldsymbol{E} + \boldsymbol{v} \times \boldsymbol{B}\right) \tag{A.1}$$

can be used to calculate the work done on a charge q by the electric field $\boldsymbol{E}$ and magnetic field $\boldsymbol{B}$. The infinitesimal amount of work dW corresponding to moving a charge an infinitesemal distance $d\boldsymbol{l}$ is then given by

$$\begin{aligned} dW &= \boldsymbol{F} \cdot d\boldsymbol{l} && \text{(A.2)} \\ &= q\left(\boldsymbol{E} + \boldsymbol{v} \times \boldsymbol{B}\right) \cdot d\boldsymbol{l} && \text{(A.3)} \\ &= q\left(\boldsymbol{E} + \boldsymbol{v} \times \boldsymbol{B}\right) \cdot \boldsymbol{v} dt && \text{(A.4)} \\ &= q\boldsymbol{E} \cdot \boldsymbol{v} dt && \text{(A.5)} \end{aligned}$$

Here it is assumed that magnetic contributions are negligible. If a spatially constant electron density ρ is assumed, the work per unit volume w can be expressed as

$$\begin{aligned} dw &= \rho \boldsymbol{E} \cdot \boldsymbol{v} dt && \text{(A.6)} \\ &= \boldsymbol{E} \cdot \boldsymbol{J} dt && \text{(A.7)} \\ &= \sigma \|\boldsymbol{E}\|^2 dt. && \text{(A.8)} \end{aligned}$$

Here Ohm's law for the current density $\boldsymbol{J} = \sigma \boldsymbol{E}$ is used, where σ stands for the conductivity. With this, the instantaneous power per unit volume p absorbed by an electron gas is $p = \sigma \|\boldsymbol{E}\|^2$. It can now be applied to free electrons in a material irradiated by a laser. Assume that whenever the gas absorbs enough energy for one electron to excite another across the band gap, an electron collision actually happens. Also assume that the incoming wave is sinusoidal. Then the avalanche ionization rate W_{AI} is

$$\begin{aligned} W_{\mathrm{AI}} &= \langle p \rangle / U_{\mathrm{eff}} && \text{(A.9)} \\ &= \frac{\sigma}{2U_{\mathrm{eff}}} \|\boldsymbol{E}\|^2. && \text{(A.10)} \end{aligned}$$

where U_{eff} is the effective band gap. According to the Drude model for conductivity, $\sigma = \frac{e^2 \tau}{m_{\mathrm{eff}}(\omega^2 \tau^2 + 1)} \rho$, with the electron charge e, the effective mass m_{eff}, the scattering

time τ and the laser frequency ω. The avalanche ionization rate is then

$$W_{\mathrm{AI}} = \frac{e^2\tau}{m_{\mathrm{eff}}(\omega^2\tau^2+1)}\frac{\|\boldsymbol{E}\|^2}{2U_{\mathrm{eff}}}\rho \tag{A.11}$$

$$= \frac{1}{n_0 c\epsilon_0}\frac{e^2\tau}{m_{\mathrm{eff}}(\omega^2\tau^2+1)}\frac{I}{U_{\mathrm{eff}}}\rho \tag{A.12}$$

$$= \beta I\rho. \tag{A.13}$$

Here the refractive index n, the permittivity of the vaccuum ϵ_0 and the speed of light c are used to write the absolute value of the electric field in terms of the intensity I.

Appendix B Extracting the amplitude and phase from the FDTD simulation

This appendix will show the validity of the approximation made in solving the Lambert-Beer-like law $\frac{dI}{dz} = -\alpha(I)I(z)$ in Section 5.2. It shows that the intensity can scale according to $I \propto \exp(-\alpha(I)z)$. Differentiating the test solution $I(z) = A\exp(-\alpha(I)z)$ results in

$$\frac{dI}{dz} = I(z)\left(\frac{d}{dz}\left[-\alpha(I)z\right]\right) \tag{B.1}$$

$$= -I(z)\left(\alpha(I) + \frac{d\alpha}{dz}z\right) \tag{B.2}$$

$$= -I(z)\left(\alpha(I) + \frac{d\alpha}{dI}\frac{dI}{dz}z\right). \tag{B.3}$$

Carrying over the $\frac{dI}{dz}$ term from the right side to the left gives

$$\frac{dI}{dz}\left(1 + I(z)\frac{d\alpha}{dI}z\right) = -\alpha(I)I(z), \tag{B.4}$$

hence the approximation is valid only if $I(z)\frac{d\alpha}{dI}z \ll 1$. The factor $\frac{d\alpha}{dI}$ is hard to calculate exactly, due to the Keldysh ionization rate that is in $\alpha = \frac{U_{\mathrm{eff}}W_{\mathrm{SFI}}\left(1-\frac{\rho}{\rho_{\max}}\right)}{I}$. However, U_{eff}, W_{SFI}, and I are all calculated numerically for the simulation. Therefore the numerical approximation of $\frac{d\alpha}{dI} \approx \frac{\alpha[i+1]-\alpha[i]}{I[i+1]-I[i]}$ can be calculated. Fig. B.1 shows the values that the approximation term $I(z)\frac{d\alpha}{dI}z$ attains over the course of the simulation, where $\rho_{\max} \to \infty$ and $z = 500\,\mathrm{nm}$. As can be seen, the approximation is not strictly valid, especially during the peak of the pulse. This means the conductivity that is calculated is not correct for the full duartion of the simulation. However, comparing the SFI conductivity to the Drude conductivity, is can be seen that it is not of great influence anyway. For this, the simulation is run and the conductivity

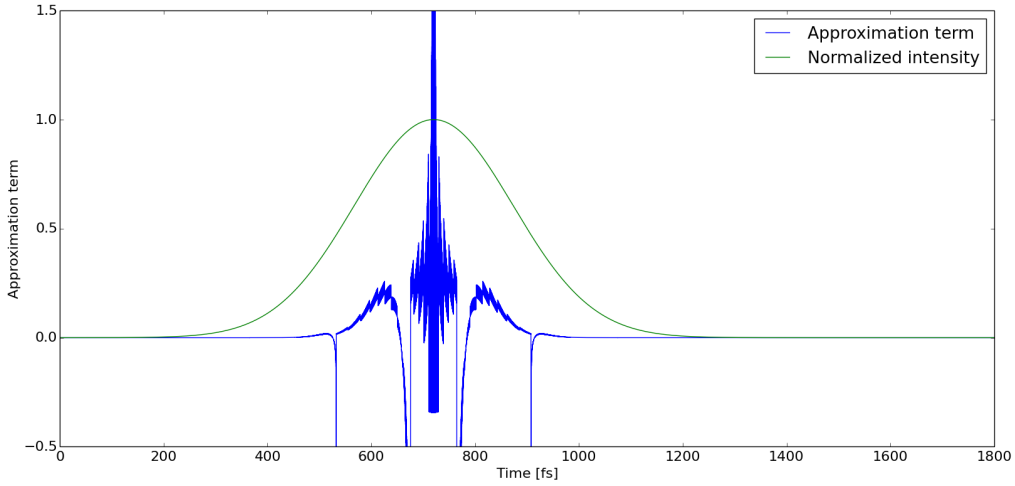

Figure B.1: In blue, the values of the approximation term $I(z)\,\frac{d\alpha}{dI}z$ during the simulation. In green, the normalized intensity.

is monitored. Between 500 fs and 9000 fs, where the approximation fails, the ratio of σ_{Drude} to σ_{SFI} is at most 0.02. Hence the influence of SFI conductivity is neglible during this time, and the approximation is taken to be valid for the entire pulse duration.

Appendix C Approximating the Lambert-Beer law

Here it is shown how to extract the amplitude and phase of the time-varying electric fields as they occur in the FDTD simulation of Section 5. Assume that the amplitude of the electric field E_0 slowly varies in time (slow wave approximation), and assume that the electric field has frequency ω_0 and phase ϕ. Then the electric field can be approximated by

$$E(t) = E_0 \cos(\omega_0 t + \phi) \tag{C.1}$$

for short enough time scales where E_0 can be taken to be constant. Now integrating $E^2(t)$ over half an optical period $T/2$ yields

$$\int_0^{T/2} E^2(t)dt = \int_0^{T/2} E_0^2 \cos^2(\omega_0 t + \phi)\, dt \tag{C.2}$$

$$= \frac{1}{4} T E_0^2. \tag{C.3}$$

Therefore

$$E_0 = \sqrt{\frac{4\int_0^{T/2} E^2(t)\, dt}{T}}, \tag{C.4}$$

in which the integral can be approximated numerically by

$$\int_0^{T/2} E^2(t)dt \cong \sum_{n=a}^{a+m} {E^n}^2 \Delta_t. \tag{C.5}$$

Here a is the starting time's index, m is the number of time steps contained in half an optical period and Δ_t is the temporal step. This way an amplitude of the electric field can be defined for every half optical period.

For calculating the phase ϕ of the electric field the integral $\int_0^{T/2} E\left(t\right) \exp\left(-i\omega_0 t\right) dt$ is considered,

$$\int_0^{T/2} E(t) \exp\left(-i\omega_0 t\right) dt = \int_0^{T/2} E_0 \cos\left(\omega_0 t + \phi\right) \exp\left(-i\omega_0 t\right) dt \tag{C.6}$$

$$= \frac{E_0}{2} \int_0^{T/2} \left[\exp\left(i\left(\omega_0 t + \phi\right)\right) + \exp\left(-i\left(\omega_0 t + \phi\right)\right)\right] \tag{C.7}$$

$$\times \exp\left(-i\omega_0 t\right) dt \tag{C.8}$$

$$= \frac{E_0 T}{4} \exp\left(i\phi\right). \tag{C.9}$$

Hence the phase of the electric field is equal to the phase of the integral $\int_0^{T/2} E\left(t\right) \exp\left(-i\omega_0 t\right) dt$, which can be evaluated numerically via a sum.

References

[1] T. Maiman, *Stimulated optical radiation in ruby*, Nature **vol. 187**, no. 4736, pp. 493–494 (1960)

[2] W. Phillips, *Nobel lecture: Laser cooling and trapping of neutral atoms*, Review of Modern Physics **vol. 70**, no. 3, pp. 721–741 (1998)

[3] L. B. Fletcher, J. J. Witcher, N. Troy, S. T. Reis, R. K. Brow, and D. M. Krol, *Effects of rare-earth doping on femtosecond laser waveguide writing in zinc polyphosphate glass*, Journal of Applied Physics **vol. 112** (2012)

[4] L. Shaw, A. Arai, S. Eaton, and P. Herman, *Waveguide writing in fused silica with a femtosecond fiber laser at 522 nm and 1 mhz repetition rate*, Optical Society of America **vol. 13**, no. 6, pp. 1999–2006 (2005)

[5] M. Ambrogi, O. Fanucchi, R. Cioni, P. Dini, A. D. Liperi, C. Cappelli, F. Davini, C. Bartolozzi, and A. Mussi, *Long-term results of radiofrequency ablation treatment of stage i non-small cell lung cancer: a prospective intention-to-treat study*, Journal of Thoracic Oncology **vol. 6**, no. 12, pp. 2044–2051 (2011)

[6] H. Zhang, *Single-shot femtosecond laser ablation on the nanoscale*, Ph.D. thesis, Utrecht University (2013)

[7] S. Wolbers, *Dynamics of femtosecond ablation on thin au film* (2013)

[8] D. Griffiths, *Introduction to Electrodynamics*, Prentice Hall (1999)

[9] P. Balling and J. Schou, *Femtosecond-laser ablation dynamics of dielectrics: Basics and applications for thin films*, Reports on Progress in Physics **vol. 76**, no. 3, p. 036502 (2013)

[10] S. Mao, F. Quéré, S. Guizard, X. Mao, R. Russo, G. Petite, and P. Martin, *Dynamics of femtosecond laser interactions with dielectrics*, Applied Physics A **vol. 79**, no. 7, pp. 1695–1709 (2004)

[11] L. Keldysh, *Ionization in the field of a strong electromagnetic wave*, Journal of Experimental and Theoretical Physics **vol. 20**, no. 5, pp. 1307–1314 (1965)

[12] V. Gruzdev and V. Komolov, *Laser-induced damage of transparent solids by femtosecond laser pulses* (2005)

[13] A. Kaiser, B. Rethfeld, M. Vicanek, and G. Simon, *Microscopic processes in dielectrics under irradiation by subpicosecond laser pulses*, Physical Review B **vol. 61**, no. 17, pp. 11437–11450 (2000)

[14] L. Sudrie, A. Couairon, M. Franco, B. Lamouroux, B. Prade, S. Tzortzakis, and A. Mysyrowicz, *Femtosecond laser-induced damage and filamentary propagation in fused silica*, Physical Review Letters **vol. 89**, no. 18, p. 186601 (2002)

[15] J. R. Peñano, P. Sprangle, B. Hafizi, W. Manheimer, and A. Zigler, *Transmission of intense femtosecond laser pulses into dielectrics*, Phys. Rev. E **vol. 72**, p. 036412, URL `http://link.aps.org/doi/10.1103/PhysRevE.72.036412` (2005)

[16] A. Wu, I. Chowdhury, and X. Xu, *Femtosecond laser absorption in fused silica: Numerical and experimental investigation*, Physical Review B **vol. 72**, p. 085128 (2005)

[17] J. Gulley, S. Winkler, and W. Dennis, *Simulation and analysis of ultrafast-laser-pulse-induced plasma generation in fused silica*, Optical Engineering **vol. 47**, no. 5, p. 054302 (2008)

[18] B. Stuart, M. Feit, A. Rubenchik, B. Shore, and M. Perry, *Laser-induced damage in dielectrics with nanosecond to subpicosecond pulses*, Physical Review Letters **vol. 74**, no. 12, pp. 2248–2251 (1995)

[19] B. Christensen and P. Balling, *Modeling ultrashort-pulse laser ablation of dielectric materials*, Physical Review B **vol. 79**, no. 15, p. 155424 (2009)

[20] S. Winkler, I. Burakov, R. Stoian, N. Bulgakova, A. Husakou, A. Mermillod-Blondin, A. Rosenfeld, D. Ashkenasi, and I. Hertel, *Transient response of dielectric materials exposed to ultrafast laser radiation*, Applied Physics A **vol. 84**, no. 4, pp. 413–422 (2006)

[21] G. Doumy, F. Quéré, O. Gobert, M. Perdrix, P. Martin, P. Audebert, J. C. Gauthier, J.-P. Geindre, and T. Wittmann, *Complete characterization of a plasma mirror for the production of high-contrast ultraintense laser pulses*, Phys. Rev. E **vol. 69**, p. 026402, URL `http://link.aps.org/doi/10.1103/PhysRevE.69.026402` (2004)

[22] P. Audebert, P. Daguzan, A. Dos Santos, J. C. Gauthier, J. P. Geindre, S. Guizard, G. Hamoniaux, K. Krastev, P. Martin, G. Petite, and A. Antonetti, *Space-time observation of an electron gas in sio_2*, Phys. Rev. Lett. **vol. 73**, pp. 1990–1993, URL `http://link.aps.org/doi/10.1103/PhysRevLett.73.1990` (1994)

[23] D. Puetro, W. Gawelda, J. Siegel, J. Bonse, G. Bachelier, and J. Solis, *Transient reflectivity and transmission changes during plasma formation and ablation in fused silica induced by femtosecond laser pulses*, Applied Physics A **vol. 92**, no. 4, pp. 803–808 (2008)

[24] B. Rethfeld, K. Sokolowski-Tinten, D. von der Linde, and S. Anisimov, *Timescales in the response of materials to femtosecond laser excitation*, Applied Physics A **vol. 79**, no. 4-6, pp. 767–769 (2004)

[25] I. H. Malitson, *Interspecimen comparison of the refractive index of fused silica*, J. Opt. Soc. Am. **vol. 55**, no. 10, pp. 1205–1209 (1965)

[26] K. Wædegaard, M. Frislev, and P. Balling, *Femtosecond laser excitation of dielectric materials: Experiments and modeling of optical properties and ablation depths*, Applied Physics A **vol. 110**, no. 3, pp. 601–605 (2012)

[27] K. Sokolowski-Tinten, J. Bialkowski, A. Cavalleri, D. von der Linde, A. Oparin, J. Meyer-ter Vehn, and S. I. Anisimov, *Transient states of matter during short pulse laser ablation*, Phys. Rev. Lett. **vol. 81**, pp. 224–227, URL `http://link.aps.org/doi/10.1103/PhysRevLett.81.224` (1998)

[28] J. Hernandez-Rueda, J. Siegel, M. Garcia-Lechuga, and J. Solis, *Femtosecond laser-induced refractive index changes at the surface of dielectrics: quantification based on newton ring analysis*, J. Opt. Soc. Am. B **vol. 31**, no. 7, pp. 1676–1683 (2014)

[29] K. S. Yee, *Numerical solution of initial boundary value problems involving maxwell's equations in isotropic media*, IEEE Trans. Antennas and Propagation pp. 302–307 (1966)

[30] D. Sullivan, *Electromagnetic Simulation Using the FDTD Method*, Wiley-IEEE Press (2000)

[31] R. Sutherland, *Handbook of Nonlinear Optics*, Optical Science and Engineering, Taylor & Francis (2003)

[32] B. Stuart, M. Feit, S. Herman, A. Shore, and M. Perry, *Nanosecond-to-femtosecond laser-induced breakdown in dielectrics*, Physical Review B **vol. 53**, no. 4, pp. 1749–1761 (1996)

[33] J. Schneider, *Understanding the Finite-difference Time-domain Method* (2010)

[34] V. V. Temnov, K. Sokolowski-Tinten, P. Zhou, A. El-Khamhawy, and D. von der Linde, *Multiphoton ionization in dielectrics: Comparison of circular and linear polarization*, Phys. Rev. Lett. **vol. 97**, p. 237403, URL `http://link.aps.org/doi/10.1103/PhysRevLett.97.237403` (2006)

[35] Q. Sun, H.-b. Jiang, Y. Liu, Z.-x. Wu, H. Yang, and Q.-h. Gong, *Diagnose parameters of plasma induced by femtosecond laser pulse in quartz and glasses*, Frontiers of Physics in China **vol. 1**, no. 1, pp. 67–71, URL `http://dx.doi.org/10.1007/s11467-005-0016-2` (2006)

[36] D. Arnold, E. Cartier, and D. J. DiMaria, *Acoustic-phonon runaway and impact ionization by hot electrons in silicon dioxide*, Phys. Rev. B **vol. 45**, pp. 1477–1480, URL `http://link.aps.org/doi/10.1103/PhysRevB.45.1477` (1992)

[37] B. Rethfeld, *Unified model for the free-electron avalanche in laser-irradiated dielectrics*, Physical Review Letters **vol. 92**, p. 187401 (2004)